Joint inversion estimate of regional glacial isostatic adjustment in Antarctica considering a lateral varying Earth structure (ESA STSE Project REGINA)

Ingo Sasgen,[1] Alba Martín-Español,[2] Alexander Horvath,[3] Volker Klemann,[4] Elizabeth J. Petrie,[5] Bert Wouters,[6] Martin Horwath,[7] Roland Pail,[3] Jonathan L. Bamber,[2] Peter J. Clarke,[8] Hannes Konrad[9] and Mark R. Drinkwater[10]

[1]*Division of Climate Sciences, Alfred Wegener Institute, Bussestraße 24, D-27570 Bremerhaven, Germany. E-mail: ingo.sasgen@awi.de*
[2]*School of Geographical Sciences, University of Bristol, University Road, Clifton, Bristol BS8 1SS, United Kingdom*
[3]*Institut für Astronomische und Physikalische Geodäsie, Technische Universität München, Arcisstraße 21, D-80333 München, Germany*
[4]*Department of Geodesy, GFZ German Research Centre for Geosciences, Telegrafenberg, D-14473 Potsdam, Germany*
[5]*School of Geographical and Earth Sciences, University of Glasgow, Glasgow G12 8QQ, United Kingdom*
[6]*Institute for Marine and Atmospheric Research, Utrecht University, Princetonplein 5, 3584 CC, Utrecht, The Netherlands*
[7]*Institut für Planetare Geodäsie, Technische Universität Dresden, Helmholtzstr.10, D-01069 Dresden, Germany*
[8]*School of Civil Engineering and Geosciences, Newcastle University, Newcastle NE1 7RU, United Kingdom*
[9]*School of Earth and Environment, University of Leeds, Leeds LS2 9JT, United Kingdom*
[10]*Mission Science Division, European Space Agency, European Space Research and Technology Centre, Keplerlaan 1, Noordwijk 2201 AZ, The Netherlands*

SUMMARY
A major uncertainty in determining the mass balance of the Antarctic ice sheet from measurements of satellite gravimetry, and to a lesser extent satellite altimetry, is the poorly known correction for the ongoing deformation of the solid Earth caused by glacial isostatic adjustment (GIA). Although much progress has been made in consistently modeling the ice-sheet evolution throughout the last glacial cycle, as well as the induced bedrock deformation caused by these load changes, forward models of GIA remain ambiguous due to the lack of observational constraints on the ice sheet's past extent and thickness and mantle rheology beneath the continent. As an alternative to forward-modeling GIA, we estimate GIA from multiple space-geodetic observations: Gravity Recovery and Climate Experiment (GRACE), Envisat/ICESat and Global Positioning System (GPS). Making use of the different sensitivities of the respective satellite observations to current and past surface-mass (ice mass) change and solid Earth processes, we estimate GIA based on viscoelastic response functions to disc load forcing. We calculate and distribute the viscoelastic response functions according to estimates of the variability of lithosphere thickness and mantle viscosity in Antarctica. We compare our GIA estimate with published GIA corrections and evaluate its impact in determining the ice-mass balance in Antarctica from GRACE and satellite altimetry. Particular focus is applied to the Amundsen Sea Sector in West Antarctica, where uplift rates of several centimetres per year have been measured by GPS. We show that most of this uplift is caused by the rapid viscoelastic response to recent ice-load changes, enabled by the presence of a low-viscosity upper mantle in West Antarctica. This paper presents the second and final contributions summarizing the work carried out within a European Space Agency funded study, REGINA (www.regina-science.eu).

Key words: Glaciology; Global change from geodesy; Gravity anomalies and Earth structure; Loading of the Earth; Antarctica; Joint inversion.

1 INTRODUCTION

The largest uncertainty in mass balance estimates for the Antarctic ice sheet (AIS) from gravimetric techniques is caused by the poorly known viscoelastic deformation of the solid Earth in response to past changes in glacial loads (e.g. Shepherd *et al.* 2012, suppl.).

The mass movement in the Earth's interior associated with this glacial isostatic adjustment (GIA) causes an apparent mass change, which has to be separated and removed from the Gravity Recovery and Climate Experiment (GRACE) signal of present ice-mass change using a GIA estimate. The total magnitude of this correction for Antarctica lies between 50 and 200 Gt yr^{-1} depending on the

model assumptions (Martín-Español *et al.* 2016b), and is comparable in magnitude to the ice-dynamic imbalance observed today (e.g. Rignot *et al.* 2011b). The rates of bedrock uplift associated with GIA are typically below 1 cm yr^{-1}, and are considerably smaller than the typical range of ice elevation rates ranging from decimetres to metres per year measured with satellite altimetry. Nevertheless, when integrated over the entire ice sheet, GIA causes a systematic bias in the altimetry data, which has to be corrected. In contrast, vertical deformations of the Earth surface measured by the global navigation satellite systems are significantly affected by GIA (e.g. Thomas *et al.* 2011).

Two principal approaches exist for estimating GIA. First, forward-modeling GIA by forcing a viscoelastic Earth model with an ice-loading history (Wu & Peltier 1982; Nakada & Lambeck 1988; Peltier 1994; Kaufmann 2002; Peltier 2004), which can either be based on a numerical ice-sheet model responding to climate forcing (Whitehouse *et al.* 2012), or reconstructed from geomorphological observations of ice thickness (Ivins & James 2005). A combination of both reconstruction methods is also possible (e.g. Tarasov *et al.* 2012). This approach is henceforth called GIA forward modeling. Second, it is possible to estimate GIA from multiple geodetic measurements with different sensitivities to GIA and present-day ice-mass change processes (Wahr *et al.* 2000; Velicogna & Wahr 2002; Riva *et al.* 2009; Wu *et al.* 2010; Gunter *et al.* 2014; Martín-Español *et al.* 2016a)—henceforth called GIA inversion estimate. Although much progress has been achieved in numerical modeling of the coupled ice/solid Earth system (e.g. Gomez *et al.* 2013; Konrad *et al.* 2015), as well as in the coverage of Global Positioning System (GPS) data (Bevis *et al.* 2009) and interpretation of the long-term trends in the satellite data, large differences remain between the various GIA solutions, causing substantial uncertainty in GRACE ice-mass balances for Antarctica (Martín-Español 2016b).

In this study, we derive a new empirical GIA estimate for Antarctica by the inversion of multiple space-geodetic observations. We advance this approach, compared to previous efforts (e.g. Gunter *et al.* 2014), through a reassessment of the input data sets (REGINA paper I—Sasgen *et al.* 2017), including an updated and augmented data set of GPS uplift rates, and by basing the joint inversion on local viscoelastic response functions, allowing us to account for known lateral variations in the Earth structure of Antarctica. Our approach, based on viscoelastic response functions, is also different from the Bayesian estimation scheme presented in Martín-Español *et al.* (2016a), and allows us to address, in particular, the large uplift rates presumably enabled by low upper-mantle viscosities in West Antarctica.

As was done in a more recent study (Martín-Español *et al.* 2016a), we include GPS uplift rates in addition to GRACE and altimetry data. This allows us to reduce the influence of the *a priori* snow/ice density distribution which is necessary to convert elevation changes to mass changes. In addition, we refine the assumption of an average rock density, transitioning from shelf to continental areas, applied in the work of Riva *et al.* (2009) and Gunter *et al.* (2014) for converting GIA-induced geoid-height rate to radial displacement rate. Unlike some other studies, we do not pre-define regional spatial patterns (Sasgen *et al.* 2013) or length scales (Martín-Español *et al.* 2016a) of the expected GIA signal. Instead, to account for the dynamics of the GIA process, we base our combination on viscoelastic response functions to a disc load forcing for an ensemble of Earth structures, representing the laterally heterogeneous lithosphere thickness and mantle viscosity in Antarctica (e.g. Morelli & Danesi 2004).

This paper first presents the combination method we have developed and applied, then summarizes the preparation of the input data sets and the viscoelastic response functions, which are described in detail in REGINA paper I (Sasgen *et al.* 2017). Finally, we discuss the GIA estimate and its impact on GRACE and altimetry measurements derived mass and volume balances, and compares the estimates to previously published GIA corrections.

2 METHOD

2.1 Formulation of problem

The separation of present-day ice-mass change and GIA is enabled by the different sensitivities of the satellite observations with respect to present and past load changes (Fig. 1). In the following, m_{pd}, denotes present-day mass changes of the ice sheet, as the net balance of snow accumulation, ablation and ice-dynamic flow, while m_{past} denotes mass changes of the ice sheet that occurred in the past (before our observation period) and cause GIA. The parameter h_c denotes changes in the firn air content caused by firn compaction (see Ligtenberg *et al.* 2014). Firn compaction decreases the firn air content (with no mass change), lowering the surface elevation (and thus volume) of the ice sheet, but it has no effect on gravity or bedrock elevation. Here, the rate of firn compaction is subtracted from the elevation rates from altimetry as the final processing step of the altimetry data set. More details are provided in REGINA paper I (Sasgen *et al.* 2017). In contrast, snow accumulation is considered by the spatial distribution of the mean surface density obtained from RACMO2/ANT. The spatial distribution of regions of snow accumulation and regions dominated by ice dynamics constitutes our snow/ice density mask, ρ used to relate altimetry and gravimetry signals (see Section 3.4.1).

Since the GIA signal, the target of this study, occurs at an approximately constant rate over the time span of the satellite observations, we restrict ourselves to considering linear rates of change. That is, the parameters m_{pd}, m_{past} and h_{comp} denote linear rates of change. Likewise, the observations from altimetry, gravimetry and GPS are incorporated in terms of linear rates of change, adjusted to the original observation time-series. Details of the determination of the optimal linear trends for each data set are described in REGINA paper I (Sasgen *et al.* 2017).

The considered observations are rate of geoid-height change, y^g, rate of bedrock uplift, y^u, and rate of surface-ice elevation change, y^h. With the conceptual separation of m_{pd}, m_{past} and h_{comp} the observation equations can be arranged in the following system of linear equations:

$$\begin{pmatrix} y^g \\ y^u \\ y^h \end{pmatrix} = \begin{pmatrix} F_e & F_v & 0 \\ G_e & G_v & 0 \\ H_e & G_v & E_w \end{pmatrix} \begin{pmatrix} m_{pd} \\ m_{past} \\ h_{comp} \end{pmatrix}, \qquad (1)$$

where $F_{e|v}$ represents the elastic | viscoelastic response functions for the rate of geoid-height change, $G_{e|v}$ represents the elastic | viscoelastic response function for the rate of bedrock uplift, E_w stands for the (filtered) equivalent water-height change. The response function $H_e = E_w/\rho + G_e$ for the elevation change (here, ice-sheet topography) is obtained by applying the snow/ice density distribution (Section 3.4.1) and correcting for associated elastic surface deformation ($E_w \gg \rho G_e$). The viscoelastic response functions F_v and G_v depend on the timing of the load change and the Earth model parameters, such as the thickness of the elastic lithosphere and the mantle viscosity structure. For a fixed temporal evolution
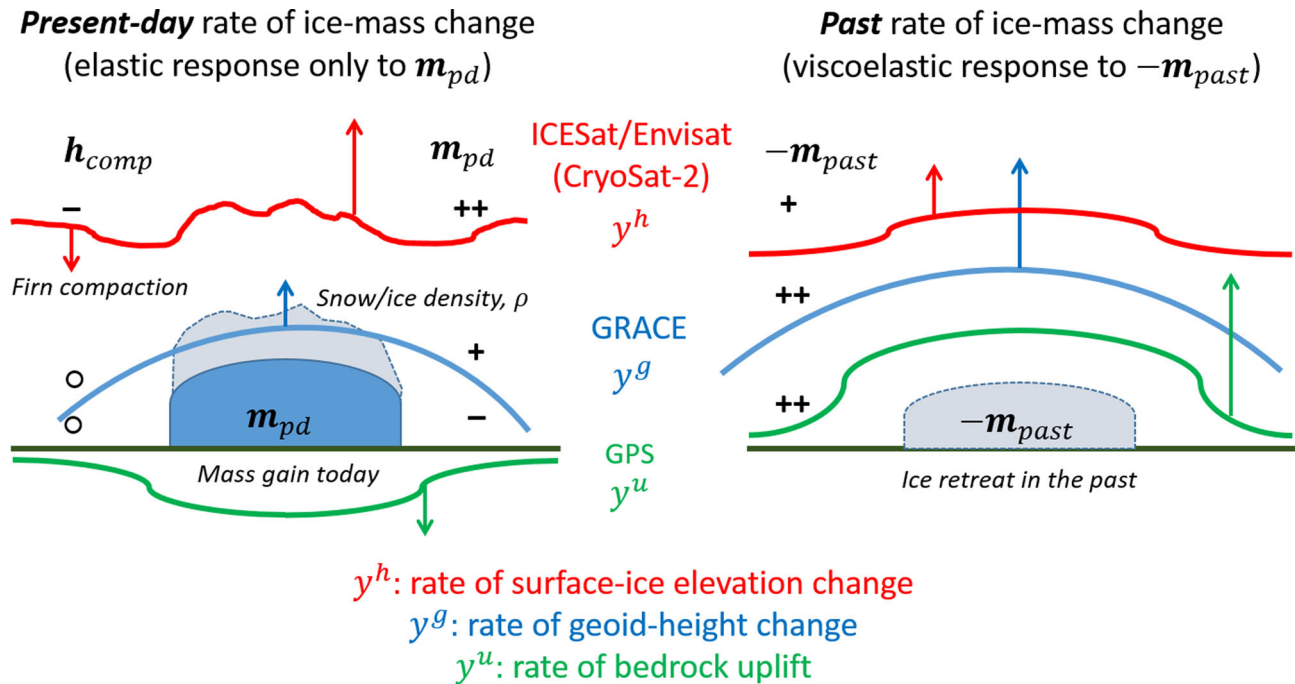
Present-day rate of ice-mass change
(elastic response only to m_{pd})

Past rate of ice-mass change
(viscoelastic response to $-m_{past}$)

h_{comp} m_{pd} ICESat/Envisat (CryoSat-2) y^h $-m_{past}$

− ++ +

Firn compaction   Snow/ice density, ρ

++

GRACE y^g

+

○ − ++

m_{pd}

○

GPS y^u

$-m_{past}$

Mass gain today   Ice retreat in the past

y^h: rate of surface-ice elevation change
y^g: rate of geoid-height change
y^u: rate of bedrock uplift

Figure 1. Concept of separating present-day rates of ice-mass change, m_{pd}, and past rates of ice-mass change, m_{past}, inducing GIA. Shown are the sign and sensitivity of the rate of elevation change, rate of gravity-field change and rate of bedrock displacement, y^h, y^g and y^u, respectively, to changes in m_{pd} and m_{past}, as well as to the rate of firn compaction, h_{comp}. Sensitivities are indicated as ++ high positive, + positive, − negative and ○ no sensitivity.

of the load and a specific set of Earth model parameters, the elastic and viscoelastic responses are linear functions of the magnitude of the load, m_{past}. This is a consequence of the linearized theory of a Maxwell-viscoelastic continuum adopted here. The elastic response functions F_e and G_e are based on the Preliminary Reference Earth Model (Dziewonski & Anderson 1981). For details on the generation of the viscoelastic response functions, see REGINA paper I (Sasgen *et al.* 2017).

The aim is to determine the unknown variables m_{pd}, m_{past} and h_{comp}, based on the observations y^g, y^u and y^h. The system of equations can be solved for the three unknowns at locations where all three data types are available. However, as described later, the problem is ill-posed requiring regularization to stabilize the inversion, which is further complicated as $F_{e|v}$ and $G_{e|v}$ are of different spatial smoothness. Here, we apply a Tikhonov L_2 regularization (e.g. Tikhonov & Arsenin 1977), providing smooth solution vectors, m_{pd}, m_{past} and h_{comp}; the optimal regularization parameter λ is determined based on the misfit between observed and predicted measurements, $\|y^u - \hat{y}^u\| + \|y^g - \hat{y}^g\|$ (see Supporting Information, SI). In addition, to overcome the limitations of the spatial coverage of the GPS data, the combination follows a two-step approach. First, gravity and altimetry trends are combined assuming the elevation rates are purely caused by present mass changes, m_{pd}. In a second step, GPS uplift rates, clustered according to the spatial GRACE resolution, are included to provide a correction on the estimate of m_{pd}, which is then updated in an iterative procedure. The scheme of the iterative procedure is shown in Fig. 2.

The estimates are performed on a geodesic grid (ICON 1.2 grid, status year 2007) used for the Max-Planck-Institute general circulation model (e.g. Wan *et al.* 2013); grid cells are represented by circular discs of averaged equal area corresponding to a radius of 63 ± 1 km. The signals for the Antarctic continent are obtained by rotating the axisymmetric load and response functions to the coordinates of the geodesic grid, and subsequent superposition. The

distribution of discs (total number: 1175) is limited to the areas confined by present-day grounding line and shelf outlines of Antarctica (continent: 1022 discs; ice shelves: 153 discs; see SI).

2.2 Step 1: combination of GRACE and Envisat/ICESat

First, we combine y^g and y^h, for the time period 2003–2009, similar to the approach presented in Gunter *et al.* (2014). For this, we correct the ice elevation changes for firn compaction h_{comp} using output of the firn compaction model of Ligtenberg *et al.* (2011). The remaining ice elevation changes are assumed to be related to snow and ice thickness changes of varying density. This reduces eq. (1) to

$$\begin{pmatrix} y^g \\ y^h \end{pmatrix} = \begin{pmatrix} F_e & F_v \\ H_e & G_v \end{pmatrix} \begin{pmatrix} m_{pd} \\ m_{past} \end{pmatrix}. \qquad (2)$$

Furthermore, in this first step, viscoelastic deformation underlying the altimetry measurement is neglected, such that $G_v = 0$, as rates of ice elevation changes driven by surface processes are on the order of tens to hundreds of millimetres per year, while the GPS-measured uplift rates are typically at the level of a few millimetres per year, even though they can reach up to 30 mm yr^{-1} in the Amundsen Sea Embayment (e.g. Groh *et al.* 2012). With these assumptions, m_{pd} can directly be estimated from $y^h = H_e m_{pd}$. The gravity field change caused by GIA to past load changes then becomes

$$F_v m_{past} = y^g - (F_e m_{pd}), \qquad (3)$$

which is then solved for m_{past} in a least-squares sense with Tikhonov regularization. This is considered as our first-order GIA estimate and similar to the solution presented in eq. (1) of Gunter *et al.* (2014). It relies on the assumptions that firn compaction has successfully been removed from the altimetry data and that the *a priori* snow/ice density mask is correct.
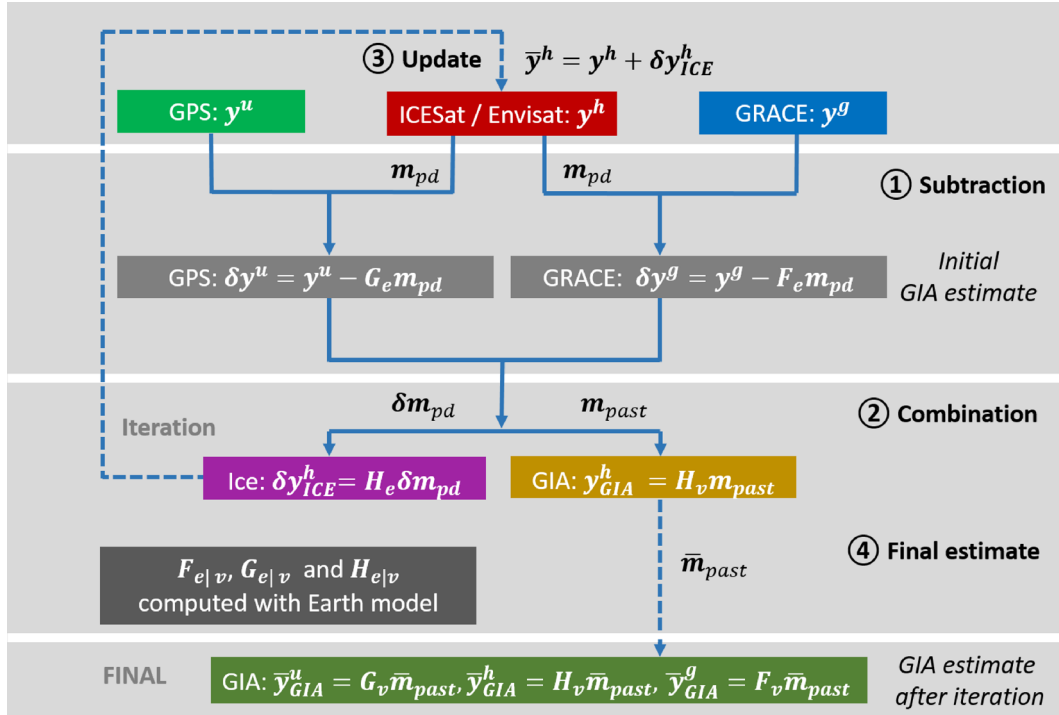
Figure 2. Scheme for combining GRACE, Envisat/ICESat and GPS data. Step 1 involves producing a first-order GIA estimate based on subtracting present-day ice-mass change inferred from altimetry from the GRACE gravity field trends. In Step 2, GPS uplift rates (corrected for the elastic effect based on altimetry) are used to separate residual present-day ice-mass change from GIA; the residual present-day ice-mass change is then used to locally improve altimetry field describing present-day ice-mass change.

Similarly, the GPS rates are corrected for elastic deformation based on the mass changes inferred from altimetry $y^u - (G_e m_{pd})$. It should be noted that instead of applying m_{pd} to elastic response functions in Step 1, high-resolution uplift rates are calculated from the altimetry field using the density mask and surface load Love numbers (spherical-harmonic cut-off degree 512). The difference between both approaches is, however, minor for most GPS sites and has a negligible impact on the final GIA estimate.

2.3 Step 2: including GPS rates

Similarly, to the gravity field trends in Step 1, the GPS rates are corrected for elastic deformation based on the mass changes inferred from altimetry $y^u - (G_e m_{pd})$. It should be noted that instead of applying m_{pd} to elastic response functions in Step 1, high-resolution uplift rates are calculated from the altimetry field using the density mask and surface load Love numbers (spherical-harmonic cut-off degree 512 and corresponding spatial half-wavelength of *ca.* 40 km). The difference between both approaches is, however, minor for most GPS sites and has a negligible impact on the final GIA estimate.

Next, to improve the first-order GIA estimate obtained in Step 1, residual present-day ice-mass changes are identified by including GPS uplift rates in this step as follows. Let $\delta y^g = y^g - F_e m_{pd}$ and $\delta y^u = y^u - G_e m_{pd}$ be the residual GRACE and GPS trends after subtracting the first-order estimates of present-day mass changes, m_{pd}. The δm_{pd}, previously unaccounted for, may arise from poor coverage in the altimetry data, an incorrect snow/ice density mask, or an inadequate correction for firn compaction. Then, an update of the present-day mass change, δm_{pd} and the past mass change, m_{past}, can be estimated by solving the reduced system of linear equations,

$$\begin{pmatrix} \delta y^g \\ \delta y^u \end{pmatrix} = \begin{pmatrix} F_e & F_v \\ G_e & G_v \end{pmatrix} \begin{pmatrix} \delta m_{pd} \\ m_{past} \end{pmatrix}. \qquad (4)$$

Here, the complementarity of the response functions with respect to present-day and past mass changes is of advantage. For example, a measured signal with positive uplift and negative gravity field change will be, at least in parts, caused by present-day ice-mass changes and the associated elastic response. Eq. (4) allows estimating this remaining present-day ice-mass change and updating the GIA estimation accordingly.

Due to the sparse distribution of the GPS data, and to avoid an underdetermined system of equations, it is necessary to reduce the observation and solution domain to the k_{max} grid locations (here, $k_{max} = 42$) closest to the GPS or mean GPS site positions of the clustered data (see Section 3.2), respectively, $\delta y^{g|u} = \{y_k^{g|u}\}$ and $\delta m_{pd | past}^k = \{m_{pd | past}^k\}$, for $k = 1, 2, \ldots, k_{max}$. Note that the corrections $m_{pd | past}^k$ determined at the GPS locations, affect the solution only in an area governed by spatial wavelength of the respective response function.

Next, we update the first-order estimate of the surface-ice elevation change from altimetry based on the residual present-day ice-mass change we estimated with eq. (4), according to $\hat{y}^h = y^h + \delta y_{ICE}^h = y^h + H_e \delta m_{pd}$. Note that here H_e is a matrix of dimension $k_{max} \times i_{max}$ relating the mass change at the GPS location k to elevation rate of each disc on the geodesic grid, i.

We now replace y^h with $\hat{y}^h$ (update the present-day ice-mass change estimate of the previous step) and repeat Steps 1 and 2 until the updates of δy_{ICE}^h are negligible, which is achieved after about three iterations in our final GIA estimate, $\hat{y}_{GIA}^g = F_v \hat{m}_{past}$, and $\hat{y}_{GIA}^{u|h} = G_v \hat{m}_{past}$, where the $\hat{m}_{past}$ refers to the final past mass change estimate.
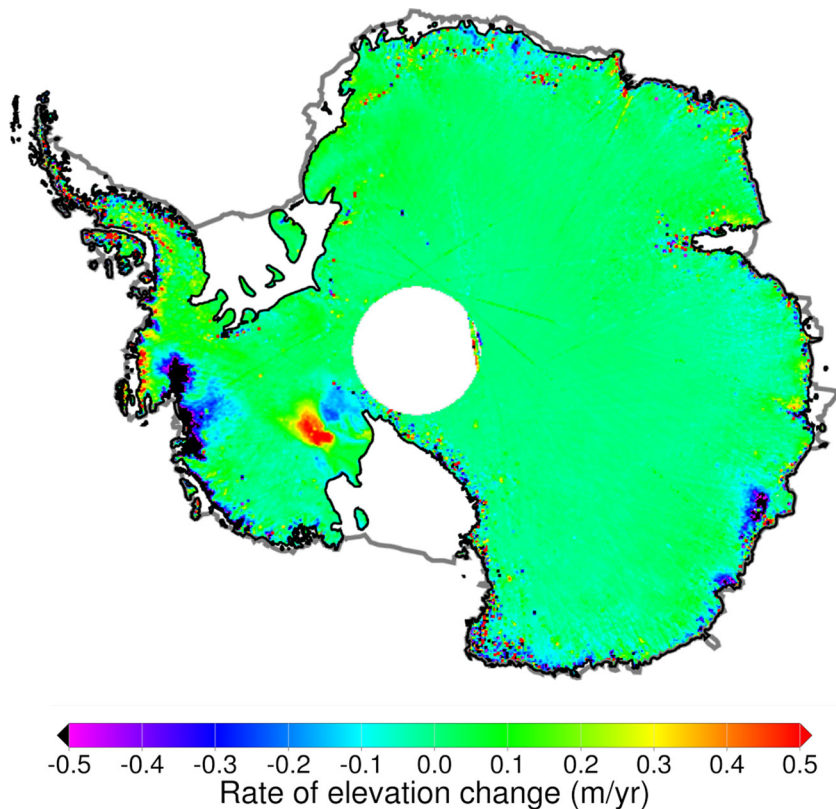
Figure 3. Envisat/ICESat rate of elevation change for 2003–2009 (m yr^{-1}). Data are corrected for the rate of firn compaction, h_{comp}, based on firn compaction module of RACMO2/ANT (Ligtenberg *et al.* 2011). Effects from snow accumulation are not removed. For details see REGINA paper I (Sasgen *et al.* 2017).

3 INPUT DATA SETS

3.1 Altimetry

Rates of elevation change y^h of the ice sheet are obtained from laser and radar altimeters of ICESat and Envisat, respectively, for the coeval time interval 2003 February to 2009 October. We use both data sets to improve the spatial and temporal coverage afforded by their combination. To test the stationarity of the recovered GIA estimate, we extend the time-series up to 2013 December by including CryoSat-2 rates of elevation change for the years 2010–2013 (Helm *et al.* 2014). We also use the prolonged time-series of the altimetry data sets to assess the impact of our GIA estimate on volume balance estimates. Details on the processing of the altimetry data sets are provided in REGINA paper I (Sasgen *et al.* 2017).

We determine ICESat elevation rates y^h based on release 33/633 data from 2003 February until 2009 October (Abshire *et al.* 2005). To estimate elevation change rates, we use multivariate regression to fit rectangular planes to near repeat tracks of ICESat measurements (Howat *et al.* 2008) from which topographic slope (both across and along tracks) and y^h are simultaneously estimated.

For Envisat radar altimetry, time-series of height changes are provided by Flament & Rémy (2012), based on an along-track approach. Elevation trends were estimated every 1 km along track, by binning all the echoes within a 500 m radius and then fitting a 10-parameter least-squares model in order to correct for the across-track topography and changes in snowpack properties (Flament & Rémy 2012).

Elevation changes from both ICESat and Envisat data were gridded into a 10 × 10 km grid on a polar-stereographic projection (central latitude 71°S; central longitude 0°W and origin at the South

Pole). To increase the coverage and reliability of the y^h estimate, we produce a combination of elevation rates based on both data sets. For each grid cell, the elevation rate was estimated from the data set with the smaller standard error. In this way, elevation rates over areas with steep topography and along the ice-sheet margins were mainly derived from ICESat, while Envisat was chosen over some flat areas and regions where ICESat data were not present (see fig. 1.1 from Sasgen *et al.* 2017). After the combination, we apply a correction for the rate of firn densification obtained from the firn deification model of Ligtenberg *et al.* (2011), driven by RACMO2/ANT.

3.2 GPS uplift rates and clustering algorithm

The GPS processing strategy is similar to that of Thomas *et al.* (2011), but with more recent processing software (GIPSY-OASIS 6.2) and background model updates included, and covering the time interval 1995.0–2013.7. A mini ensemble of processing runs was also performed to improve understanding of potential systematic processing errors. The processing strategy and ensemble, as well as the rate estimation are described in full detail elsewhere (see Sasgen *et al.* 2017). Rates are in ITRF2008, which is defined to realize zero translations and translation rates with respect to the mean Earth centre of mass (Altamimi *et al.* 2011). A summary of the processing strategy on uplift rates, and comparisons with uplift rates from earlier studies are given in REGINA paper I (Sasgen *et al.* 2017). Note that we do not correct for Antarctic bedrock displacement related to co- and post-seismic deformation following large earthquakes, for example, intraplate Earthquake of 1998 with a magnitude of ~8.2 (Nettles *et al.* 1999; King & Santamaría-Gómez
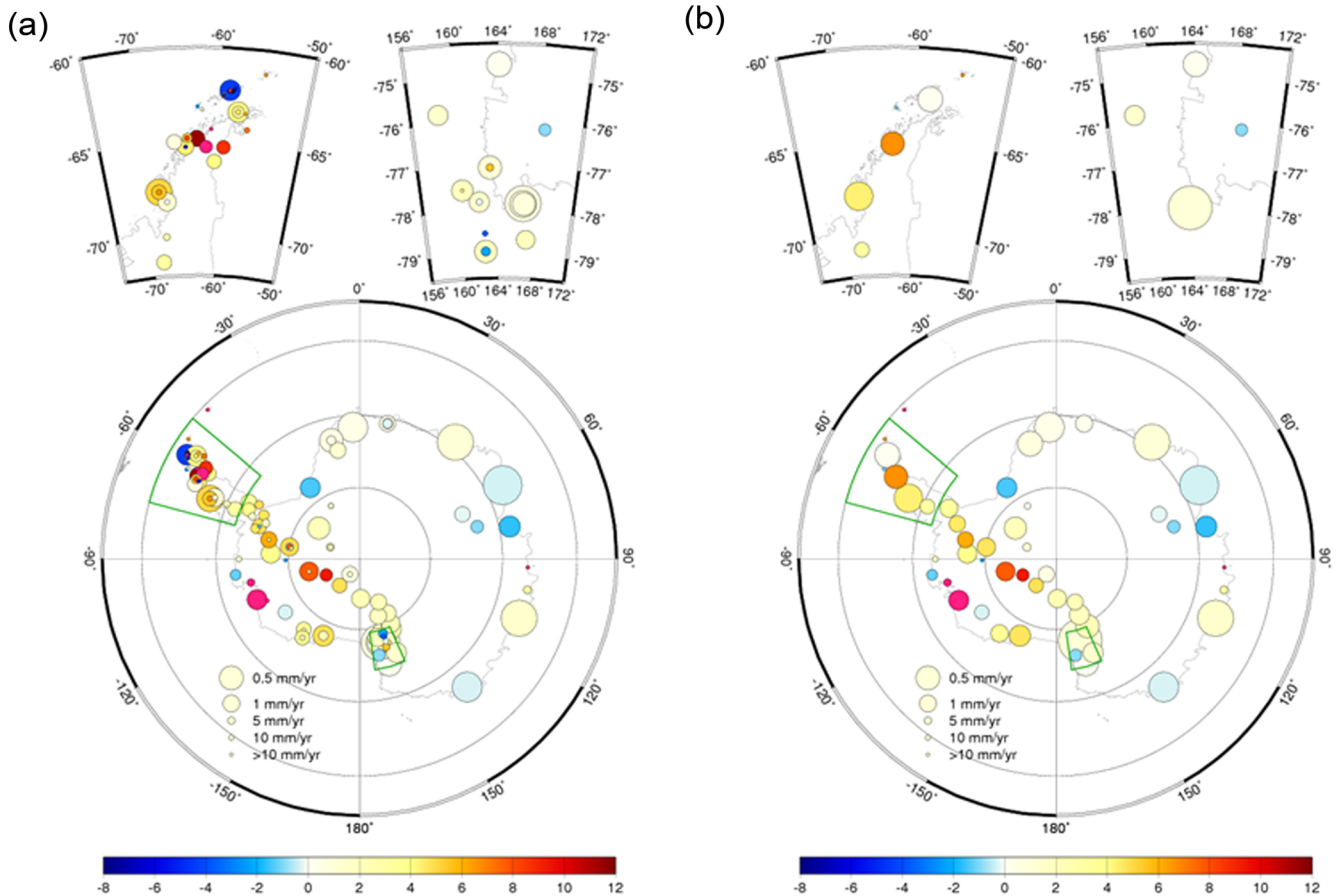
Figure 4. Uplift rates in Antarctica, for (a) 108 available GPS sites, and (b) 42 clusters after application of the clustering algorithm with a threshold distance of 200 km. Symbol colour denotes uplift rate (mm yr^{-1}) and symbol area denotes 1σ confidence limit

2016). The potential influence on our GIA estimate is discussed in Section 4.1.

We now build regional clusters of the estimated uplift rates at the 118 Antarctic GPS sites. The rationale for this is the observation that neighbouring sites with discrepant uplift rates often have large formal errors because the rates are based on campaign data or short measurement time spans. In addition, the GIA signature is expected to have a regional characteristic. Differences between observed uplift rates of accurate sites in close proximity may be caused by (small) changes in elastic accumulation or local tectonics, that is, geophysical noise, not by local variability in GIA. Because we perform the joint inversion on a grid with node distances of *ca.* 120 km, and GRACE and filtered altimetry input data sets with a spatial resolution of about 200 km (half-wavelength), we have no need for individual uplift rate estimates for sites separated by only a few tens of kilometres. Instead, we consider a weighted average of nearby sites to be more robust.

The clustering algorithm operates as follows; for each threshold distance in turn (here: 10, 20, 50, 100, 150, 200 and 220 km), independent pairs of sites/clusters closer to each other than this threshold distance are merged by calculating the weighted mean of their uplift rates, and the simple mean of the site/cluster positions. The procedure is repeated until no new pairs created by these mergers are found within the threshold, and then the threshold is increased and iteration is restarted. Fig. 4 shows the results of the clustering with 200 km maximum threshold, which is the preferred choice for the joint inversion, considering the GRACE resolution (spatial

half-wavelength of 200 km). It is evident that the main regional characteristics of the uplift rates recovered with GPS are retained, while discrepant sites at the same or nearby locations are merged, considering their respective uncertainties, to a representative average. The similar smoothness of the deformation field from GPS and the GRACE gravity field avoids the occurrence of artefacts in the inversion. The number of clusters with the 200 km maximum threshold is 42 (from individual 118 sites). Note that the clustering is carried out on the initial data set, representing elastic and viscoelastic uplift rates.

3.3 Gravimetry

We calculate the linear trend of the gravity field over Antarctica, expressed apparent water column of surface-mass change, y^g, by adjusting a multiparameter model (constant, linear trend, annual and semi-annual harmonic amplitudes) within the time period 2003 February to 2009 October (coeval to Envisat/ICESat measurement period). This time-series is derived from monthly Stokes coefficients from GRACE, up to degree and order 50 corresponding to a spatial half-wavelength of 200 km, provided by the Center for Space Research (CSR; Bettadpur 2012), release 5. Consistent with the GPS processing, the GRACE reference frame is ITRF2008. We reduce the typical north–south correlated error structures in GRACE monthly solutions by adapting the de-striping filter of Swenson & Wahr (2006, Swenson filter) to the region of Antarctica. Chambers & Bonin (2012) have previously performed a similar filter
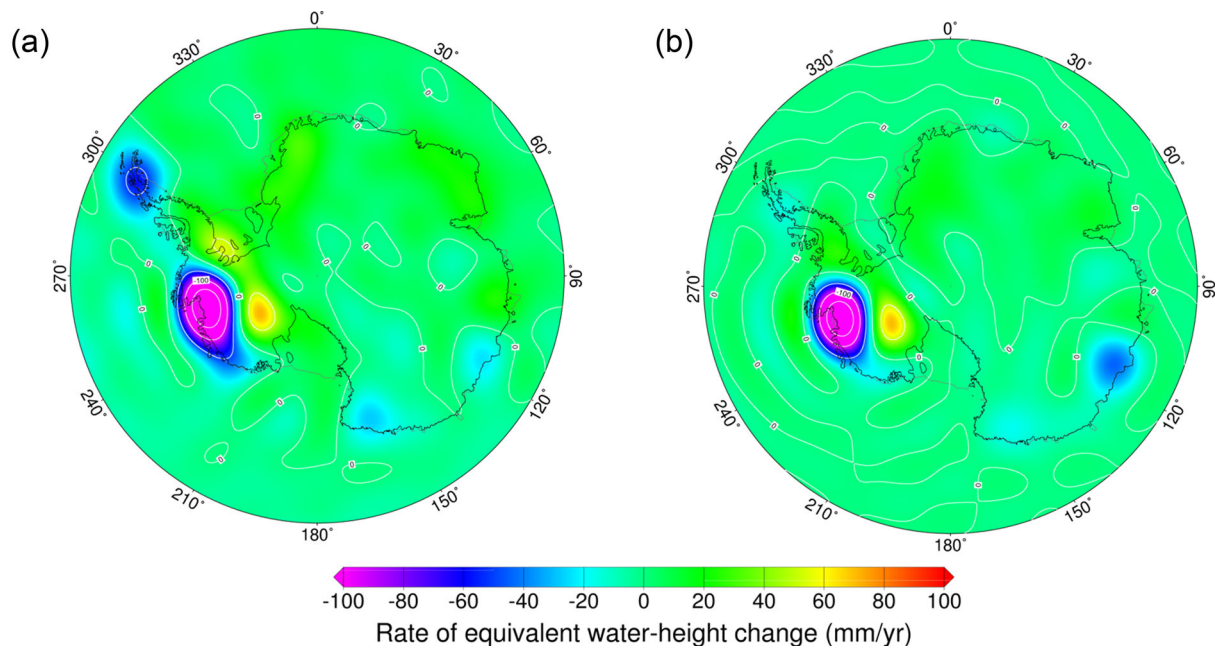
Figure 5. Rate of surface-mass change for the time period 2003–2009 from (a) GRACE (CSR release 05) with the optimized Swenson & Wahr (2006) and 200 km Gaussian filtering and (b) Envisat/ICESat applying the snow/ice density distribution shown in Fig. 3 and filtering similar to the GRACE trends (Gaussian filter of 200 km half-width). The spherical-harmonic cut-off degree and order is 50. The surface-mass change is expressed as millimetre water-equivalent (mm w.e.) yr^{-1}.

enhancement for global oceanic signals. We optimize the trade-off between (i) the signal corruption of synthetic data, and (ii) the effectivity of the noise reduction, inferred by filtering the residual GRACE minus altimetry trends south of 60°S. This residual is considered an upper bound for the uncertainty of the GRACE uncertainty. The optimal values for the Swenson filter minimize the quadratic sum of signal corruption and residual noise. For details see REGINA paper I (Sasgen *et al.* 2017).

In a second step, to increase the robustness of the temporal linear trends, non-linear (de-trended) surface-mass variations associated with snow accumulation events are reduced from the GRACE monthly solutions. For this purpose, we convert the surface-mass balance (SMB) of the regional atmosphere and climate model RACMO2/ANT (Lenaerts *et al.* 2012) into monthly sets of spherical-harmonic coefficients representing the storage changes of the ice sheet. After de-correlation with the optimized Swenson filter and the reduction of the non-linear mass components, the remaining noise is suppressed with a Gaussian filter of 200 km, which is estimated as the optimal half-width by applying the Wiener optimal filter (Sasgen *et al.* 2006). Since the quality of GRACE monthly solutions varies over time, for example, due to evolving orbital sampling patterns, information on time-dependent error levels is introduced by month-dependent weighting in the estimation of the linear trends (e.g. Rangelova & Sideris 2008). Formal uncertainties of the trend are estimated based on the residual signal (after the multiparameter adjustment). This error estimate does not account for serial correlation of the residuals. Williams *et al.* (2014) report that such serial correlation increases the uncertainty of trends by factors typically on the order of 2, but sometimes reaching 6. The resulting linear trend, as well as the altimetry data filtered similar to GRACE is shown in Fig. 5.

Based on comparing signals over the continent and the ocean, Williams *et al.* (2014) suggest that a large part of the serial correlation is due to actual ice-mass variability and not caused by errors of the GRACE observing system. To reduce such autocor-

relation of residuals, we subtract modeled surface-mass balance (SMB) fluctuation effects prior to estimating the trends, leading to a smaller residual and, hence, smaller empirical uncertainties of the trend. More details are found in Sasgen *et al.* (2017), even though a thorough investigation on the effectiveness of the SMB to reduce residual autocorrelation is yet to be undertaken. Nonetheless, in the actual inversion procedure (Section 2), we adopt an uncertainty estimate that is more pessimistic: we chose the deviations between trends from different GRACE release, which are typically larger than the uncertainties derived for a single release.

3.4 Auxiliary data

3.4.1 Snow/ice density estimate

We use a snow/ice density distribution (Fig. 6) for converting the elevation rates derived from Envisat/ICESat altimetry to surface-mass rates during Step 1 of the GIA estimate. Similar to the procedure applied in Riva *et al.* (2009), the snow/ice density mask is constructed as follows: elevation changes within regions with surface-ice velocities >100 m yr^{-1} or surface-elevation rates $|y^h| > 0.3$ m yr^{-1} are assigned the density of ice, while for the remaining regions the mean surface density is obtained from RACMO2/ANT for the time period 1979–2010 (Lenaerts *et al.* 2012). The surface-ice velocity field is a combination of InSAR velocities (Rignot *et al.* 2011a) and balance velocities (Bamber *et al.* 2000). The temporal coverage of the InSAR product is 1996–2011 (https://nsidc.org/data/docs/measures/nsidc0484_rignot/, last accessed 22 September 2017).

The construction of our density mask follows the rationale that high, localized elevation rates are typically associated with fast glacier flow or strong glacier thinning and retreat, while broader patterns of moderate elevation change are dominantly driven accumulation variations. The additional threshold criterion attributing to $|y^h| > 0.3$ m yr^{-1}, the density of ice accounts to some extent
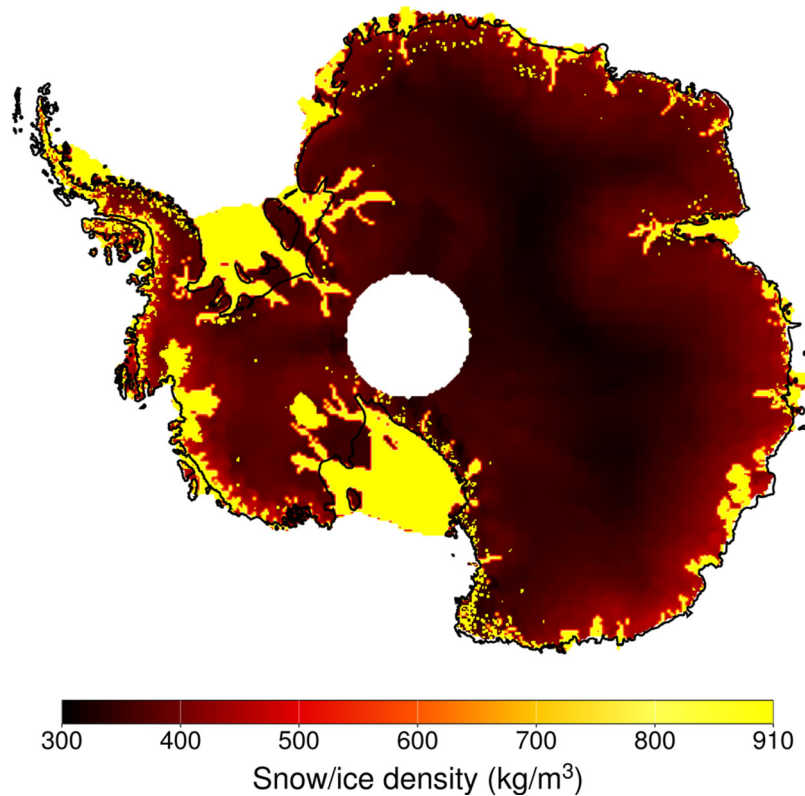
Figure 6. Snow/ice density distribution applied to the rates of elevation change from altimetry, during Step 1 of the GIA estimation.

for ice-dynamic thinning that has occurred since the surface-ice velocities have been measured (1996–2011; Rignot *et al.* 2011a). An exception is made for the Kamb Ice Stream (Ice stream C), where dynamic elevation changes are known to occur in spite of low velocities (Retzlaff & Bentley 1993). It should be emphasized that we refrain from additionally correcting for anomalies in the surface-mass balance due to the rather short meteorological measurement records underlying RACMO2/ANT (1978–2015) and the associated problem of defining a reference climatology for Antarctica.

3.4.2 Earth structure and distribution of viscoelastic response functions

In Antarctica, properties of the Earth's lithosphere and mantle are considered to vary strongly between East and West Antarctica; while the East AIS rests on a cratonic structure, West Antarctica is dominated by a rift system. Seismic shear wave velocity anomalies support this geological inference (Morelli & Danesi 2004), indicating a much thinner elastic lithosphere, h_L, and lower upper-mantle viscosities in West Antarctica compared to East Antarctica. Here, we accommodate the rheological differences between East and West Antarctica by selecting from our ensemble of Earth structures (see REGINA paper I, Sasgen *et al.* 2017), those viscoelastic response functions that match the Earth structure model by Priestley & McKenzie (2013). In particular, we derive the thickness of the elastic lithosphere from the 3-D distribution of mantle viscosities provided by Priestley & McKenzie (2013), by assuming that lithosphere and mantle layers with viscosities $>10^{22}$ Pa s respond elastically on the considered timescale of a few millennia. The resulting thickness of the elastic lithosphere ranges from 30 km in parts of the Antarctic Peninsula, to 200 km in East Antarctica, which is a plausible range considering similar geological regimes.

Similar lithosphere thickness values (± 10 km) are obtained by applying thresholds of 10^{21} Pa s (h_L thicker) to 10^{23} Pa s (h_L thinner); however, the preferred threshold leading to the GIA estimate best fitting the data is 10^{22} Pa s (see Section S.4, SI). In equilibrium state between load forcing and deformational response, the viscoelastic response function is only governed by the thickness of the elastic lithosphere. Therefore, currently mantle viscosities are neglected in the selection of the response functions. Note, for consistency with the satellite data realized in the International Terrestrial Reference Frame (ITRF) reference frame, the response functions are calculated in the centre of mass. Although the assumption of an equilibrium state clearly does not capture the full-dynamic behaviour of GIA, we consider it a good approximation for the low-viscosity regime of West Antarctica and necessary to avoid an additional *a priori* information on the temporal evolution of the ice sheet. In contrast, the cratonic structure underneath East Antarctica suggests higher mantle viscosities and, therefore, longer relaxation times, particularly in the central part of the ice sheet (Fig. 7). However, model simulations show only moderate and slow ice thickness changes in the central part of the ice sheet, since the Last Glacial Maximum (e.g. Mackintosh *et al.* 2011), justifying the use of response functions describing the viscoelastic equilibrium state. Fig. 7 shows the lithosphere thickness derived from Priestley & McKenzie (2013), as well as the lithosphere thickness of the viscoelastic response functions attributed to each disc.

4 RESULTS

4.1 Spatial rate of radial displacement

The total rate of radial displacement, $\hat{y}^u$, obtained in the joint inversion is shown in Fig. 8, as well as its separation into the elastic and viscoelastic components of the deformation. Note that ice
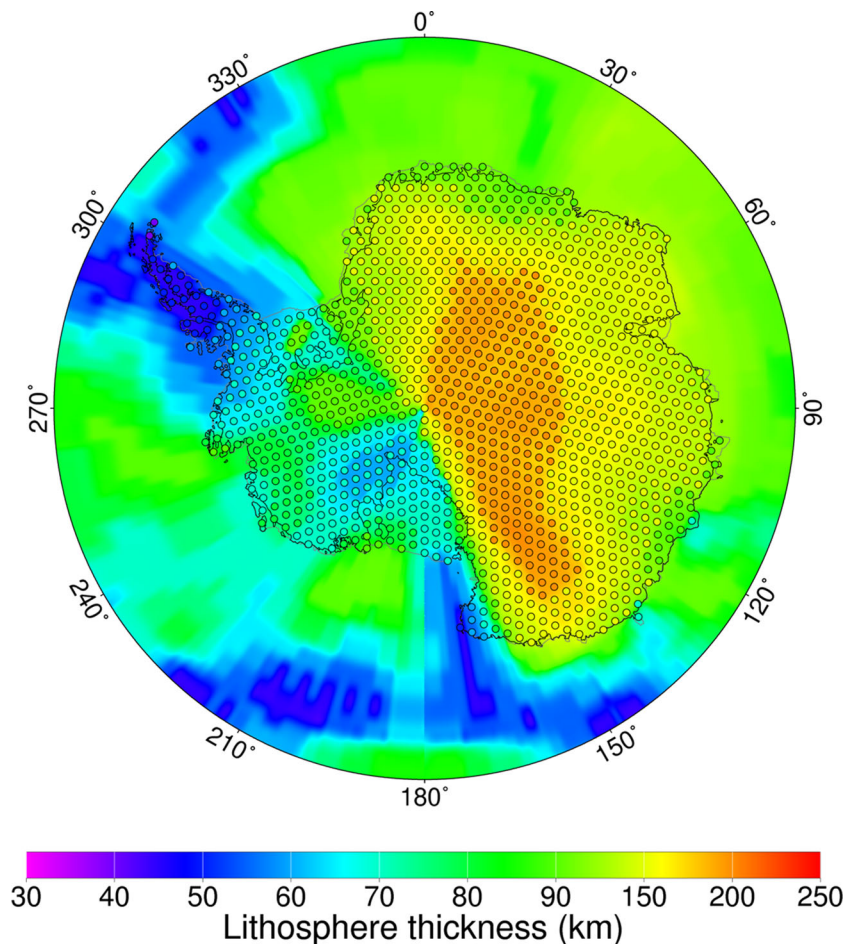
Figure 7. Thickness of elastic lithosphere (km) for the Antarctic region, as derived from Priestley & McKenzie (2013), and the thickness assigned in the inversion associated with the viscoelastic response function (circles).

shelves are assumed to be in floatation equilibrium; hence, the gravity signal recovered is attributed entirely to GIA, except where continental signals leak into the ice-shelf areas. A reference to the geographic locations of Antarctica discussed in the following can be found in Fig. 11. The strongest elastic response is localized in the Amundsen Sea Sector of West Antarctica, where large present-day mass losses cause strong rates of instantaneous rebound of the solid Earth. Localized rates of elastic uplift are also visible close to the tributary glaciers of the former Larsen B ice shelf on the Antarctic Peninsula. In contrast, bedrock subsidence is recovered in the area of the Kamb Ice Stream, caused by an increased ice build-up following the stagnation of this glacier system (Retzlaff & Bentley 1993). Large elastic rates are also visible around the GPS sites THUR, in the Bellingshausen Sea area, and SDLY, in Marie Byrd Land (see Fig. 10 for the locations of GPS sites).

The GIA-induced rates of radial displacement (Fig. 8) have two local maxima, one over the Filcher–Ronne ice shelf and one in the western part of the Amundsen Sea Embayment with rates above 10 mm yr^{-1}, which are discussed further in Section 4.3. The large uplift rates measured along the Transantarctic Mountains in central West Antarctica GPS (*ca.* 8 mm yr^{-1}) are mainly attributed to GIA, and they fill in along a stretch of uplift extending from the Ross ice shelf further inland. However, part of this signal is also attributed to elastic uplift caused by present-day snow/ice-mass changes, as seen in the altimetry data (see fig. 2 in REGINA paper I, Sasgen

et al. 2017). It should also be noted that, recently, problems of snow affecting the GPS receiver accuracy have been identified (Wilson, personal communication, 2016).

Another complication in the interpretation of GPS uplift rates arises from possible presence of co- and post-seismic bedrock deformation related to large earthquakes. King & Santamaría-Gómez (2016) have pointed out that the deformation signatures at Dumont d'Urville (DUM1), East Antarctica, contain abrupt offsets and relaxation behaviour related to the 1998 $M \sim 8.2$ Antarctica intraplate Earthquake, with the epicentre about 600 km from the station (Nettles *et al.* 1999). Furthermore, horizontal deformation associated with the 1998 earthquake has also been identified in the GPS record at Casey (CAS1), about 2000 km from the epicentre, suggesting that the deformation feature could be widespread, not only local (DeMets *et al.* 2017). At DUM1, subsidence rates changed significantly from *ca.* 0.0 ± 0.5 mm yr^{-1} (1993–1998) before the earthquake, to about -2.0 ± 1.0 mm yr^{-1} (1998–2005) immediately after the earthquake, to about -0.2 ± 0.7 mm yr^{-1} (2005–2015), after most of the post-seismic relaxation took place (taken from fig. 2 in King & Santamaría-Gómez 2016). Here, we adopt the rate of -0.3 ± 0.3 mm yr^{-1} for the full GPS record at DUM1 (1995–2013), which is similar to the value during the Envisat/ICESat period (2003–2009) of -0.2 ± 0.7 mm yr^{-1}. It is also in agreement with the value of 0.0 ± 0.5 mm yr^{-1} (1993–1998; before the earthquake), put forward by King & Santamaría-Gómez (2016) to be the most reliable.
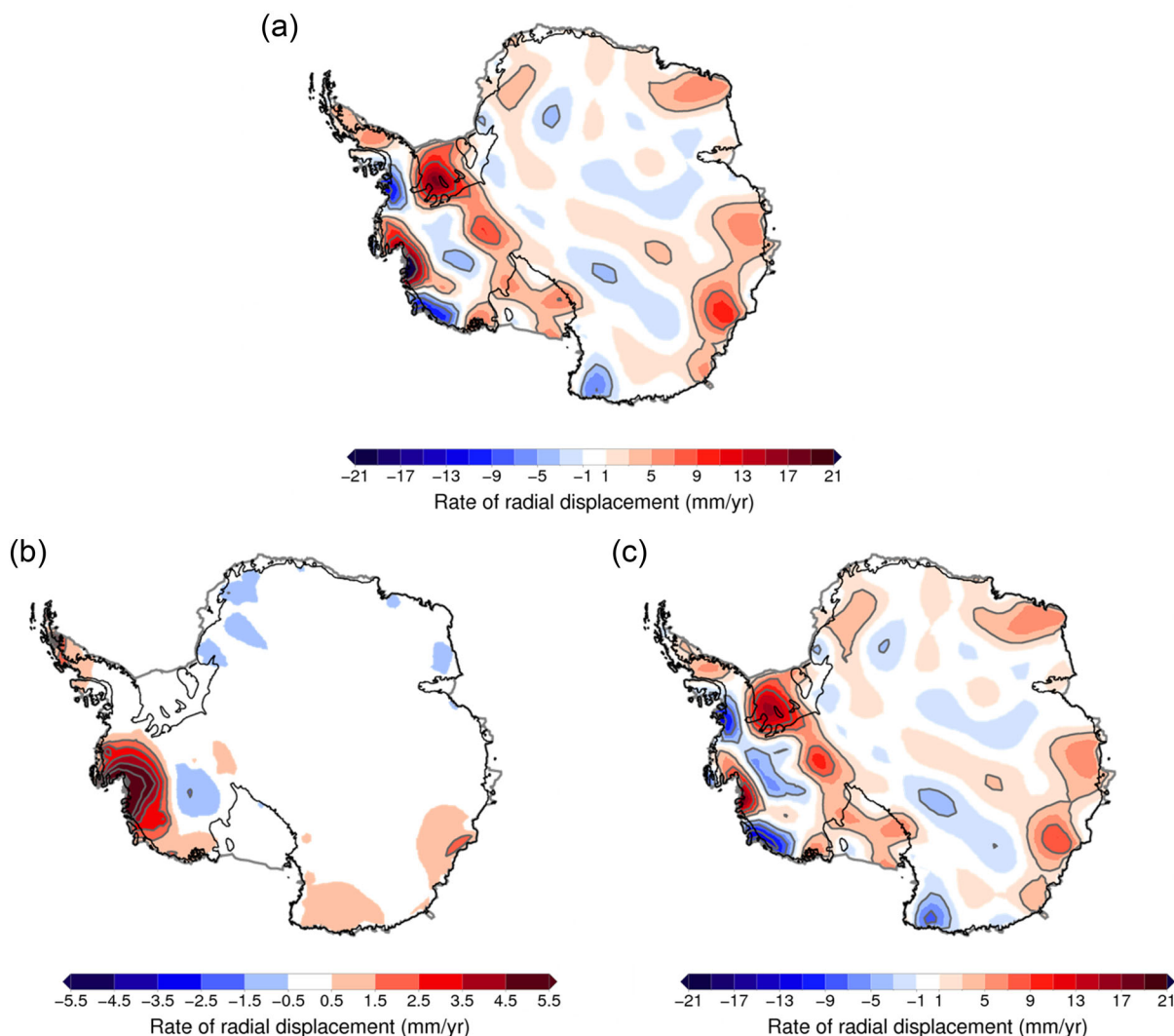
Figure 8. Rate of radial displacement (mm yr^{-1}) for (a) present-day ice-mass change and GIA (total), (b) present-day ice-mass change (elastic) and (c) the REGINA estimate of GIA (viscoelastic). Note different colour scale in (b).

East Antarctica shows uplift rates close to zero, however with some fluctuations of positive and negative rates. Contiguous, large-scale subsidence predicted by many models due to the increase of accumulation in the Holocene caused by the warming atmosphere and the associated increase in the water content and moisture transport. Subsidence in central East Antarctica is recovered in our solution, even though the stripy pattern may reflect noise. This is reflected in the rather large uncertainties for the East Antarctica presented in Section 5. The largest uplift rates are found in Wilkes Land, while Oates Land shows subsidence (geographic references are marked in Fig. 11). Most GIA corrections present a short-wavelength signal of uplift over the Totten glacier system, as a consequence of negative load change in the last 16 kyr in that region (e.g. Huybrechts 2002), supporting our GIA estimate in Wilkes Land. Note, however, that almost no ice history constraints exist for Wilkes Land to inform GIA modeling (Bentley *et al.* 2014). The signature in Oates Land, however, is likely a result of an insufficient correction for surface-mass processes due to the lack of nearby GPS stations, as well as noise in the altimetry data caused by the rugged terrain (see fig. 2 from Sasgen *et al.* 2017). A similar situation is present west of Amundsen Sea Embayment (Getz ice shelf area) and in

eastern Bellingshausen Sea area, where the recovered GIA signal shows large rates of subsidence (*ca.* 15 mm yr^{-1}). It is likely that estimates of surface-mass loss from altimetry are too low in magnitude in the Getz ice shelf area due to the complex topography, as well as the difficult discrimination between ice shelf and grounded ice, and changes thereof. As these areas are underlain by a weak Earth structure, an insufficient correction for present-day ice-mass changes leads to large and spurious uplift rates. Along the Antarctic Peninsula, the terrain has a similar complexity; there, however, GPS uplift rates are more abundant and allow empirically improving the GIA estimate.

4.2 Spatial rate of geoid-height change

The rate of geoid-height change, $\hat{y}^g$, for the total mass change (recent and GIA-induced), as well as separated into present-day ice-mass change and GIA is shown in Fig. 9. It should be stressed that the GIA-induced geoid rate is not derived by applying a conversion factor to the radial displacement field; it is derived in parallel to the radial displacement field based on the distribution of the viscoelastic response functions. For example, a locally high viscoelastic uplift
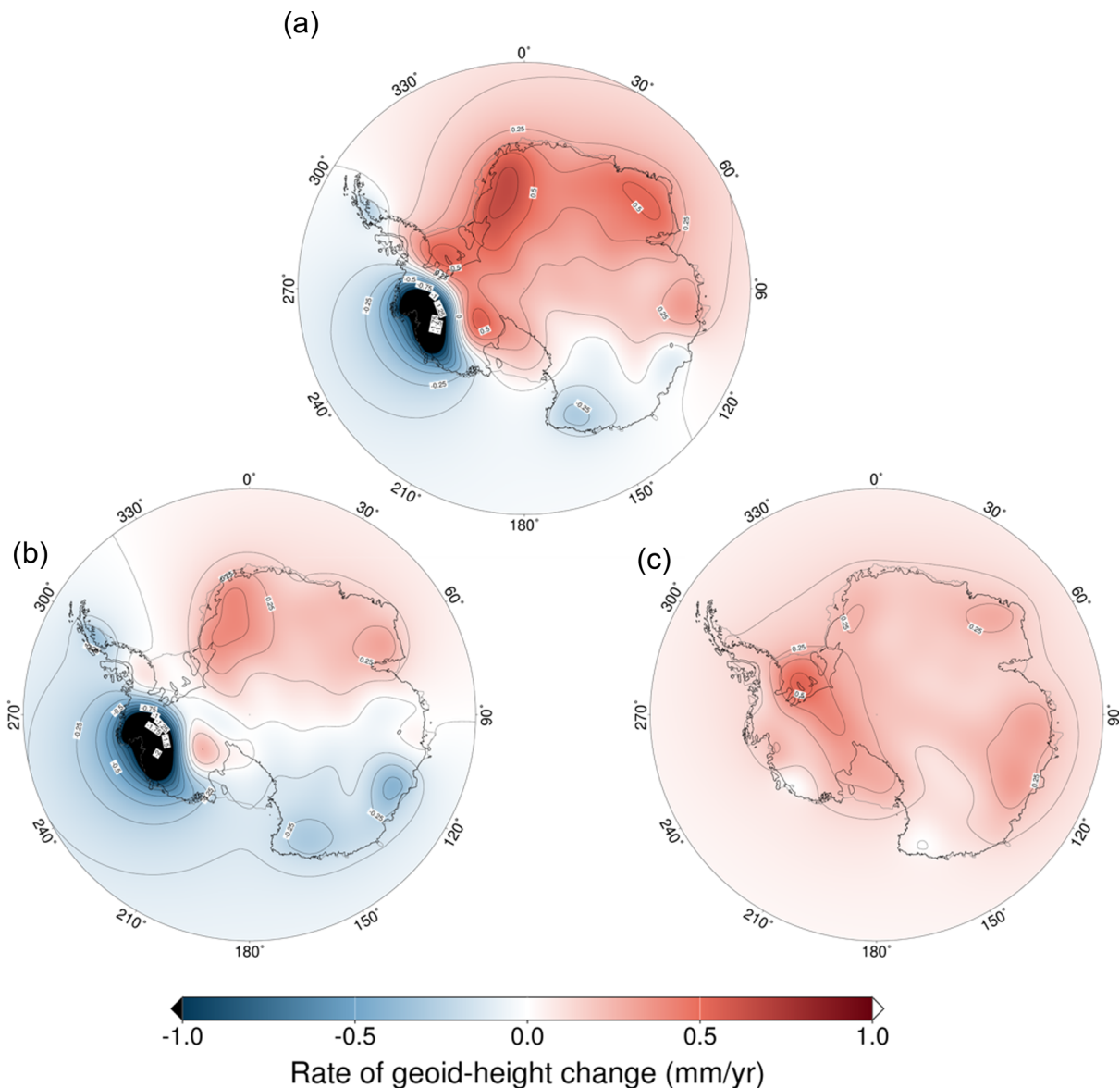
(a)

(b)

(c)

Figure 9. Rate of geoid-height change (mm yr^{-1}) for (a) present-day ice-mass change and GIA, (b) present-day ice-mass change and (c) the REGINA estimate of GIA.

rate may correspond to only a moderate increase in the geoid height, if the Earth structure attributed to this area is characterized by a thin lithosphere.

The rate of geoid height attributed to present-day surface-mass change is dominated by the mass loss currently occurring in the Amundsen Sea Embayment. Here, geoid rates are by far the largest, amounting to several mm yr^{-1}. Marked ice losses are recovered along the northern part of the Antarctic Peninsula, as well as in Wilkes Land (Totten glacier) and George V Land, whereas mass increases due to the ice-dynamic slowdown of Kamb Ice Stream. Other signals of mass increase are recovered in Dronning Maud Land and Enderby Land, which is explained by enhanced accumulation within the considered time period. All these mass anomalies are known and have been related to their causative processes (e.g. Wouters *et al.* 2014).

In contrast, the GIA-induced geoid rate is positive or close to zero over the entire continent of Antarctica, with the strongest magnitudes prevailing over West Antarctica. In East Antarctica, the radial

displacement fields (Fig. 8) show some alternation between uplift and (smaller) subsidence, whereas the associated geoid pattern is generally positive, which is due to the overlapping with of positive geoid signals arising from the coastal rim in East Antarctica. Geoid rates peak at *ca.* 0.5 mm yr^{-1} on the Filchner–Ronne ice-shelf area, but are also large for the Amundsen Sea and Ross ice shelf area, as well as in coastal East Antarctica along the western part of Wilkes Land and Enderby Land. In comparison to the present-day ice-mass changes, the recovered GIA signature has a distinct spatial pattern (peak anomalies in different locations) and it is smoother; this suggests that both signals have been successfully separated with no marked signs of correlation artefacts. In addition, the present-day ice-mass changes correspond in magnitude and spatial location to those inferred from the mass budget method (Rignot *et al.* 2008, 2011b). The GIA-induced bedrock subsidence found in the hinterland of the Getz ice shelf (Fig. 8) is much less pronounced in geoid rate due to the thin lithosphere adopted in the viscoelastic response function for this area.
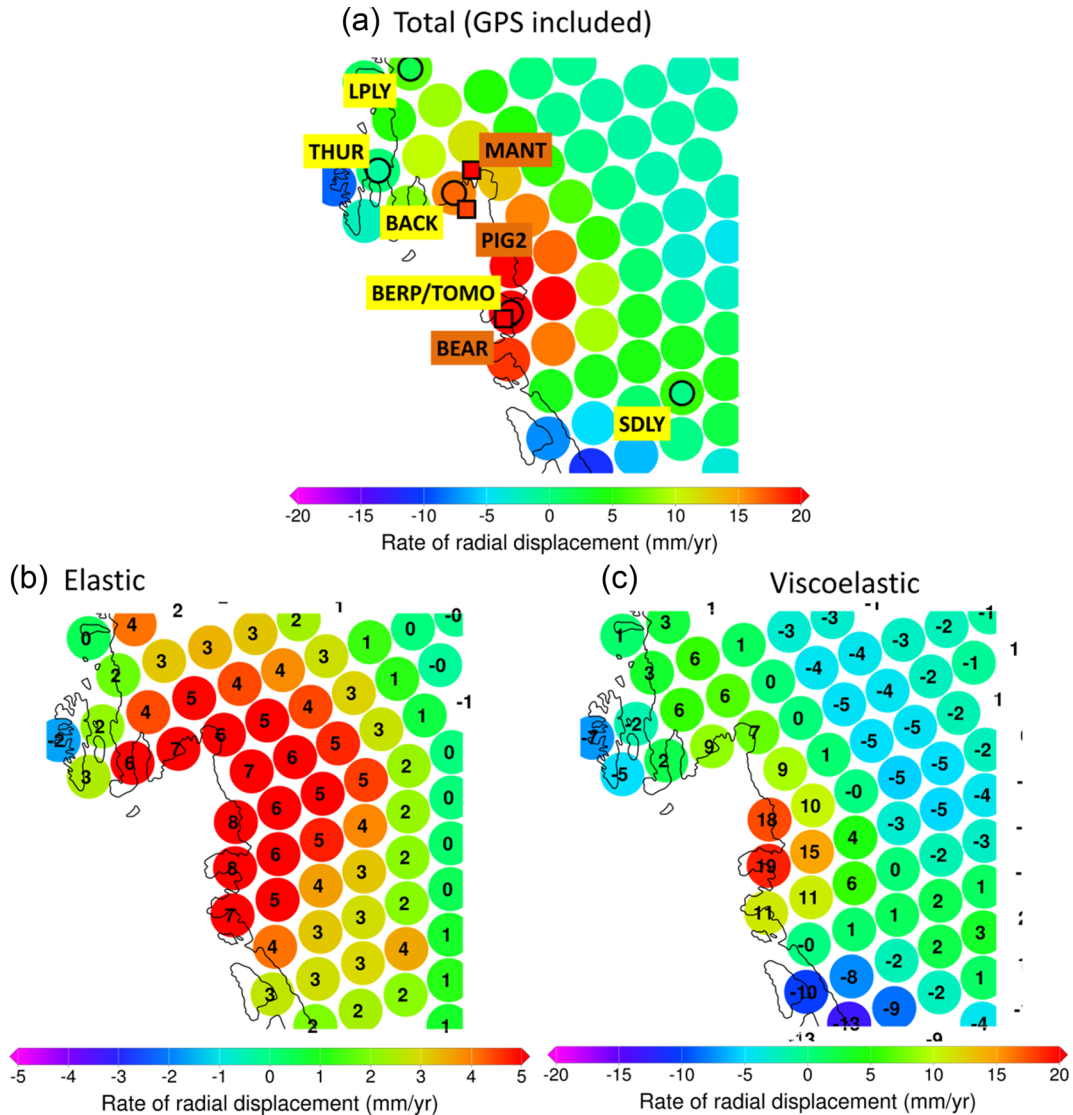
Figure 10. Rate of radial displacement (mm yr^{-1}) in the Amundsen Sea Embayment for (a) total signal (including GPS uplift rates as inset circles) comprising present-day ice-mass change and GIA, (b) present-day ice-mass change only and (c) GIA only. GPS sites used in the inversion (yellow label) are moved in location to the nearest node of the geodesic grid. Uplift rates provided by Groh *et al.* (2012) based on campaign data are shown for comparison at their true locations (brown labels). Note the different colour scale in (b). Numbers in the discs of (b) and (c) indicate the respective rates of radial displacement in millimetres per year.

4.3 Large uplift in the Amundsen Sea Embayment

Next, we pay particular attention to the interpretation of the large uplift rates at the cm yr^{-1} level measured by GPS in the Amundsen Sea Embayment; these cannot be explained solely by the elastic response to ongoing ice-mass unloading (Groh *et al.* 2012). Seismic imaging (Hansen *et al.* 2014), as well as inferences from radar sounding and subglacial water routing (Schroeder *et al.* 2014) point towards a very low viscosity in the upper mantle of this region. Therefore, the large uplift is likely caused by a rapid viscoelastic response to more recent ice retreat and thinning. Due to the lack of geomorphological and climatological constraints on the ice evolution in the past few centuries to millennia, GIA forward models typically do not reproduce this uplift signature. With the joint inversion, we are able to reconcile with the large uplift, when considering the weak Earth structure in the determination of the viscoelastic response functions for this region.

A zoom into the displacement fields of Amundsen Sea Embayment at the respective disc locations of the geodesic grid (Fig. 8) are presented in Fig. 10. Overall, the total uplift obtained from the inversion is in very good agreement with the large uplift rates measured at the GPS stations, which is an indication that the applied smoothing constraint and viscoelastic response functions used in the inversion are adequate. Note that the GPS uplift rates determined here support earlier estimates based on campaign data at BEAR, PIG2 and MANT (Groh *et al.* 2012).

Elastic uplift rates of 5–8 mm yr^{-1} are determined for most of the Amundsen Sea Sector, as a consequence of ongoing glacier retreat and thinning. The uplift increases by *ca.* 2 mm yr^{-1}, when extending the time-series from the years 2003–2009 to 2003–2013 (not shown)—this is expected due to the acceleration of ice loss in this area. The GIA-induced signature shows uplift above 6 mm yr^{-1} along the coast of the Amundsen Sea Embayment; peak rates of 18–19 mm yr^{-1} are determined in the vicinity of the Thwaites
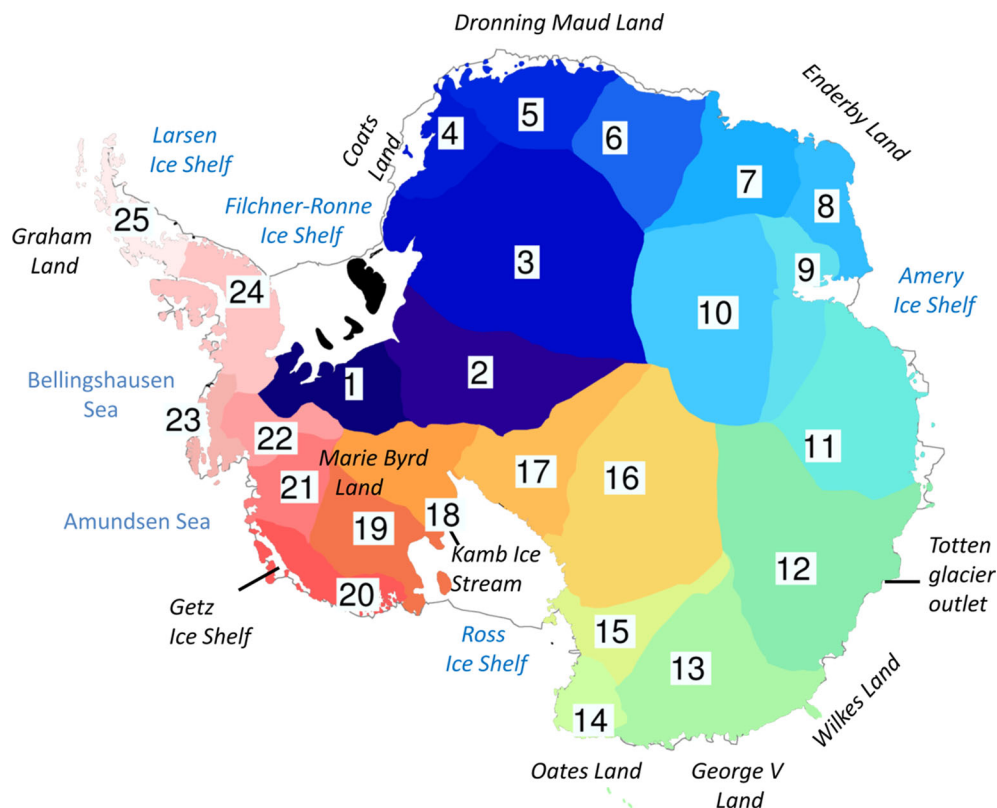
Figure 11. Outline of Antarctic drainage basins used in REGINA (after Sasgen *et al.* 2013).

and Smith/Pope/Kohler glaciers. The impact on the rate of geoid-height change is small, however, due to the thin elastic lithosphere in this region. As pointed out in the description of the viscoelastic response functions shown in REGINA paper I (Sasgen *et al.* 2017), a moderate unloading in the past may cause substantial viscoelastic uplift if resting on a thin elastic lithosphere. Moreover, for upper-mantle viscosities of *ca.* 10^{19} Pa s (An *et al.* 2015; Heezel *et al.* 2016), the relaxation is fast enough that a new equilibrium state is achieved within a few centuries. Both properties of the Earth structure prevail in West Antarctica, suggesting that the isolated GIA signals are plausible.

It should be mentioned that the total uncertainty of GIA estimate in West Antarctica is large, due to the uncertainty in the altimetry data sets and the elevation rate to mass conversion (see Fig. 14). We have high confidence in our GIA estimate where GPS, altimetry and GRACE are co-located; but the regional spatial pattern, also in coastal West Antarctic, remains to be of a large uncertainty.

5 IMPACT ANALYSIS

5.1 Impact on altimetry and gravimetry trends

Next, we evaluate the impact of the GIA estimate on volume and mass balance estimates from satellite altimetry (Envisat/ICESat and CryoSat-2) and gravimetry (GRACE) estimates for the 25 Antarctic drainage sectors shown in Fig. 11. The results are shown in Table 1. In the following, basins 2–17 are considered to be part of East Antarctica, 1 and 18–23 are West Antarctica and basins 24 and 25 form the Antarctic Peninsula. The calculation of the of the volume rate $\dot{V}_j$ for a basin is straightforward; $\dot{V}_j = \sum_i \hat{y}^u_{i,\mathrm{GIA}} A_i \alpha_i$, where i is the index of gridpoints within drainage basin j and $A_i = \mathrm{const.} =$

100 km^2 is the nominal area represented by each gridpoint (here, 10 km × 10 km Polar Stereographic grid), while α_i accounts for the distortion of the true area with respect to the nominal area ($\alpha_i = 1$ at true latitude of 71°S; range of *ca.* 0.87–1.06 within data domain). The gridded rate of radial displacement $\hat{y}^g_{\mathrm{GIA}}$ is based on the GIA estimate shown in Fig. 8, however, interpolated bilinearly from the geodesic grid to the finer Polar Stereographic grid. The apparent mass change is determined by inverting the rate of geoid-height change, $\hat{y}^g_{\mathrm{GIA}}$ (Fig. 9) to surface-mass change using a forward-modeling approach (e.g. Sasgen *et al.* 2013).

Typically, rates of ice surface-elevation change from altimetry are on the order of centimetres per year up to metres per year. In contrast, the GIA-induced bedrock uplift rates in Antarctica amount to a few millimetres per year, with a maximum of 2 cm yr^{-1} in the presence of a thin lithosphere and low viscosity in West Antarctica. Therefore, GIA is not a primary correction or uncertainty for the satellite altimetry data. Integrated over the entire ice sheet the GIA impact is below 7 per cent of the volume rates (time interval 2003–2013), for the regions with large ice loss in West Antarctica even below 2 per cent. For East Antarctica, however, the relative contribution of GIA compared to the volume rates is significant, amounting to 30 per cent (Table 1).

Importantly, the GIA-induced mass change over Antarctica is similar in magnitude to the ice-mass change recovered by GRACE for 2003–2016: here we find it to be *ca.* 40 per cent of the latter. Overall, the mass-loss rates are roughly a minimum of four times more influenced by GIA than volume rates (the ratio of ice to rock density; Table 1). The uncertainty associated with our GIA esti-mate is ±23 Gt yr^{-1} ($\sigma_{m'_{\mathrm{GIA}}}$ for 'Total' in Table 1), which is about 16 per cent of the total GRACE uncertainty budget. However, it should be kept in mind that the range of published GIA corrections is

Table 1. Apparent mean rate of volume ($\dot{V}$) change Envisat/ICESat (E/I; 2003–2009), extended with CryoSat-2 (CS-2; 2010–2013), and rate of mass ($\dot{m}$) change for GRACE (2003 January–2016 March; 152 monthly fields; CSR RL05), respectively, and the REGINA estimate for GIA-induced volume and mass change for each numbered basin in Antarctica (bold font) and uncertainties (light font).

Basin number	E/I and CS-2 (2003–2013) $\dot{V}_{altim.}$	REGINA GIA volume estimate $\dot{V}_{GIA}$.	$\sigma(\dot{V}_{GIA})$.	GRACE (2003–2016) $\dot{m}_{GRACE}$	REGINA GIA mass estimate $\dot{m}_{GIA}$.	$\sigma(\dot{m}_{GIA})$	Ice volume (2003–2013) $\dot{V}_{ice}$	Ice mass (2003–2016) $\dot{m}_{ice}$	$\sigma(\dot{m}_{ice})$
2	**−3**	**0.2**	1.3	**−2**	**4**	4	**−3**	**−6**	5
3	**24**	**0.2**	1.5	**16**	**5**	7	**24**	**11**	7
4	**13**	**0.6**	0.7	**10**	**2**	3	**12**	**7**	3
5	**14**	**0.3**	1.2	**12**	**2**	4	**14**	**11**	5
6	**20**	**0.5**	1.1	**9**	**2**	3	**20**	**7**	3
7	**6**	**1.2**	0.9	**15**	**4**	3	**5**	**12**	3
8	**7**	**0.6**	0.7	**13**	**2**	2	**6**	**11**	3
9	**3**	**−0.4**	1.2	**2**	**0**	4	**3**	**1**	4
10	**1**	**−0.1**	0.9	**3**	**0**	4	**1**	**3**	4
11	**−15**	**1.7**	1.1	**6**	**8**	3	**−17**	**−2**	4
12	**−43**	**2.6**	1.7	**−24**	**8**	6	**−46**	**−32**	7
13	**−11**	**0.1**	1.1	**0**	**1**	3	**−11**	**−1**	5
14	**12**	**−0.5**	0.9	**−7**	**−1**	2	**13**	**−5**	3
15	**−5**	**−0.2**	0.8	**1**	**0**	3	**−5**	**0**	3
16	**−3**	**−0.2**	1.1	**1**	**2**	4	**−3**	**−1**	4
17	**24**	**0.3**	1	**2**	**2**	2	**24**	**−1**	2
East Ant.	**25**	**7**	4.4	**58**	**42**	15	**18**	**16**	17
1	**−1**	**1.2**	1.3	**28**	**5**	3	**−2**	**23**	4
18	**26**	1.1	1.4	**15**	**5**	3	**25**	**10**	3
19	**−2**	**0.2**	1.7	**14**	**2**	6	**−2**	**12**	8
20	**−28**	**−0.6**	1.3	**−44**	**−3**	5	**−27**	**−41**	7
21	**−73**	**0.4**	1.6	**−62**	**2**	7	**−73**	**−65**	7
22	**−48**	**0**	1.5	**−53**	**0**	7	**−48**	**−53**	8
23	**−4**	**0.1**	1	**−12**	**0**	5	**−4**	**−13**	7
West Ant.	**−130**	**2.3**	3.8	**−115**	**12**	14	**−132**	**−127**	17
24	**−7**	**−0.1**	2.2	**−8**	**1**	9	**−7**	**−9**	10
25	**−31**	**0.1**	1	**−20**	**1**	4	**−31**	**−21**	4
Ant. Pen.	**−39**	**0**	2.4	**−28**	**2**	10	**−39**	**−30**	11
Total	**−144**	**9.4**	6.4	**−86**	**55**	23	**−153**	**−141**	27

Notes: Rate of ice-volume and ice-mass change are obtained by subtracting the GIA estimate from REGINA from the uncorrected satellite observations $\dot{V}_{altim}$ and $\dot{m}_{GRACE}$. The GRACE uncertainties (1σ) are based on error propagation considering an AR(1) model (see the text), as well as filtering and inversion errors (typically 7–10 per cent; Sasgen *et al.* 2013) and solution differences.

considerably larger than this uncertainty, with values for the associated correction of mass change ranging from *ca.* +50 to +200 Gt yr^{-1} (Martín-Español *et al.* 2016b).

Note that the analysis of GRACE time-series for the extended time period 2003–2016 involves the simultaneous estimation of offset, trend, acceleration, as well as annual and semi-annual periods and the 161 d period (tidal aliasing in GRACE due to S2 tide; Chen *et al.* 2009). Following Williams *et al.* (2014), we select an autoregressive model of order 1, AR(1), as a single stochastic model, disregarding that other models may be optimal in different regions. Nonetheless, we estimate the statistical significance of the residual lag-1 autocorrelation, and if significant, scale the uncertainties using a pre-whitening procedure (Hamed & Rao 1998). The procedure increases the uncertainties of the trend typically by a factor of around 2, except for basins 1, 9, 10, 14 and 15, where we find residual correlation not to be significant.

5.2 Comparison with published GIA corrections

Next, we compare the spatial pattern of geoid-height change obtained in this study with the published GIA forward models (Fig. 12), W12a (Whitehouse *et al.* 2012) and the GIA inversion estimate based on pre-defined regional GIA patterns, AGE1 (Sasgen *et al.* 2013). Further comparison is done for the rate of volume change

for the 25 major drainage sectors (Table 1) shown in Fig. 11, including the GIA prediction IJ05_R2 (Ivins & James 2005; Ivins *et al.* 2013), as well as the GIA estimates of Riva *et al.* (2009) and the RATES project (Martín-Español *et al.* 2016a). Note that we compare our results to Riva *et al.* (2009) instead of the updated estimate presented in Gunter *et al.* (2014), as the latter involves an *a priori* constraint on the surface-mass balance in central East Antarctica. Thus, the comparison includes two GIA corrections based on modeling (W12a and IJ05_R2), which were favoured in the ice-sheet mass balance intercomparison exercise, IMBIE (Shepherd *et al.* 2012), and two inverse estimates (AGE1 and Riva *et al.* 2009). Although these models reflect much of the variability between GIA corrections at the scale of drainage sectors (Fig. 13), this comparison is by no means exhaustive. A more extensive comparison is provided elsewhere (Martín-Español *et al.* 2016b).

The GIA-induced rate of geoid-height change as obtained by the joint inversion, and for comparison the GIA prediction W12a and the GIA estimate AGE1 is presented in Fig. 12. Note that this version of AGE1 ('GPS only', table 2 of Sasgen *et al.* 2013) is obtained by the adjustment of pre-defined GIA patterns to GPS uplift rates—no altimetry or gravimetry data were involved. All the GIA corrections show the largest uplift along a line joining the Filchner–Ronne and Ross ice shelves, West Antarctica. Also, the magnitudes of the inferred GIA are comparable and the GIA estimate of this study lies
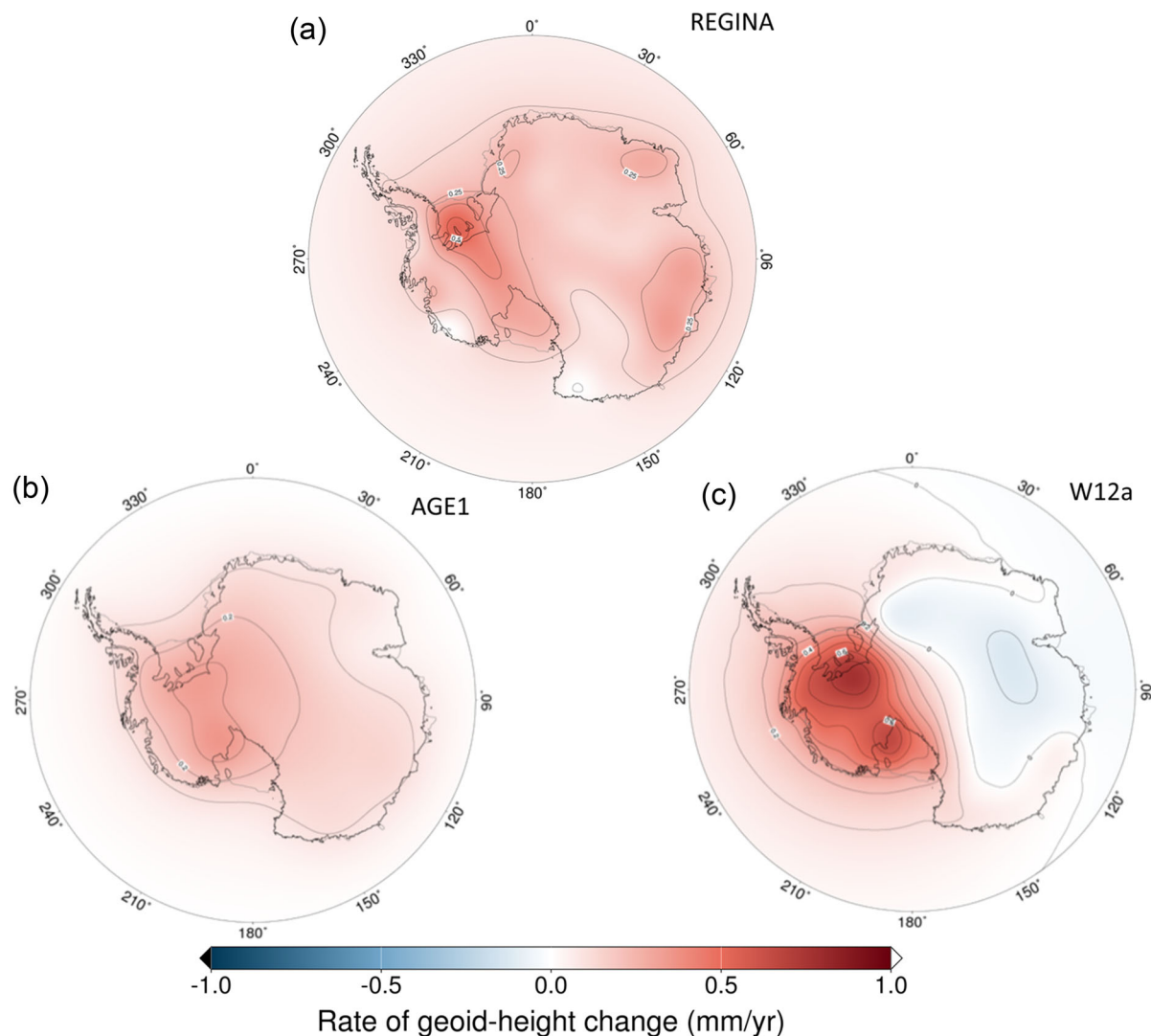
Figure 12. Spatial rate of geoid-height change (mm yr^{-1}) for (a) the GIA estimate of REGINA, (b) the GIA estimate AGE1 (Sasgen *et al.* 2013) and (c) the GIA prediction W12a (Whitehouse *et al.* 2012).

within the range provided by AGE1 and W12a. However, there are also marked differences: first, AGE1 and REGINA show a positive rate of geoid-height change over central East Antarctica, while W12 shows a decrease caused by viscoelastic subsidence due to enhanced accumulation, as a consequence of climate warming after the Last Glacial Maximum (e.g. Frieler *et al.* 2015). Therefore, a subsidence signal is most likely realistic, and also present in the GIA prediction IJ02_R2 (not shown)—even though lower in magnitude than in W12a. The accuracy of our GIA estimate depends on the availability of GPS data, which are only located along the coastal rim in East Antarctica and the uncertainty of the elevation rates in the ice-sheet interior, which may be underestimated. Therefore, a subsidence signal in central Antarctica at the millimetre level is difficult to recover with the data-driven approach presented here. Fig. 13 compares the rate of apparent ice volume change for the 25 drainage sectors for AGE1, W12a and IJ05_R2 (Riva *et al.* 2009), the inverse estimate of Martín-Español *et al.* (2016a), and the REGINA estimate of this study.

Typically, the volume rate is below 2 km^3 yr^{-1} and positive in magnitude for most drainage sectors. The exception is W12a, showing a strong negative GIA-induced volume change in Coates Land

(basin 3), the Amery ice shelf area (basin 9) and part of central East Antarctica (basin 16). As mentioned in Section 4.1, our REGINA estimate also shows subsidence signals in the Getz ice shelf area (basin 20) and Oates Land (basin 14) and, in agreement with W12a, in the Amery ice shelf area (basin 9). In general, our REGINA estimate agrees best with Riva *et al.* (2009) and RATES, which is not surprising, as their GIA correction is based on a similar inversion approach using roughly the same type of input data sets. The GIA prediction IJ05_R2 is similar in large parts of Antarctica; however, a marked difference to the REGINA estimate (and that of Riva *et al.* 2009) is the lack of uplift along Wilkes Land (basins 11 and 12), East Antarctica. This is also not supported by the GIA prediction W12a and may therefore be an artefact in our GIA estimate (and that of Riva *et al.* 2009), caused by enhanced snow accumulation in the time period, which is captured differently by GRACE and Envisat/ICESat. Although all GIA corrections provide similar rates of volume change when integrated over the entire Antarctica continent, differences at the regional level remain large. The standard deviation between the GIA corrections is 0.3 km^3 yr^{-1} on average for all drainage sectors, but sometimes it is a large as 1–2 km^3 yr^{-1}. Clearly, more research is needed to
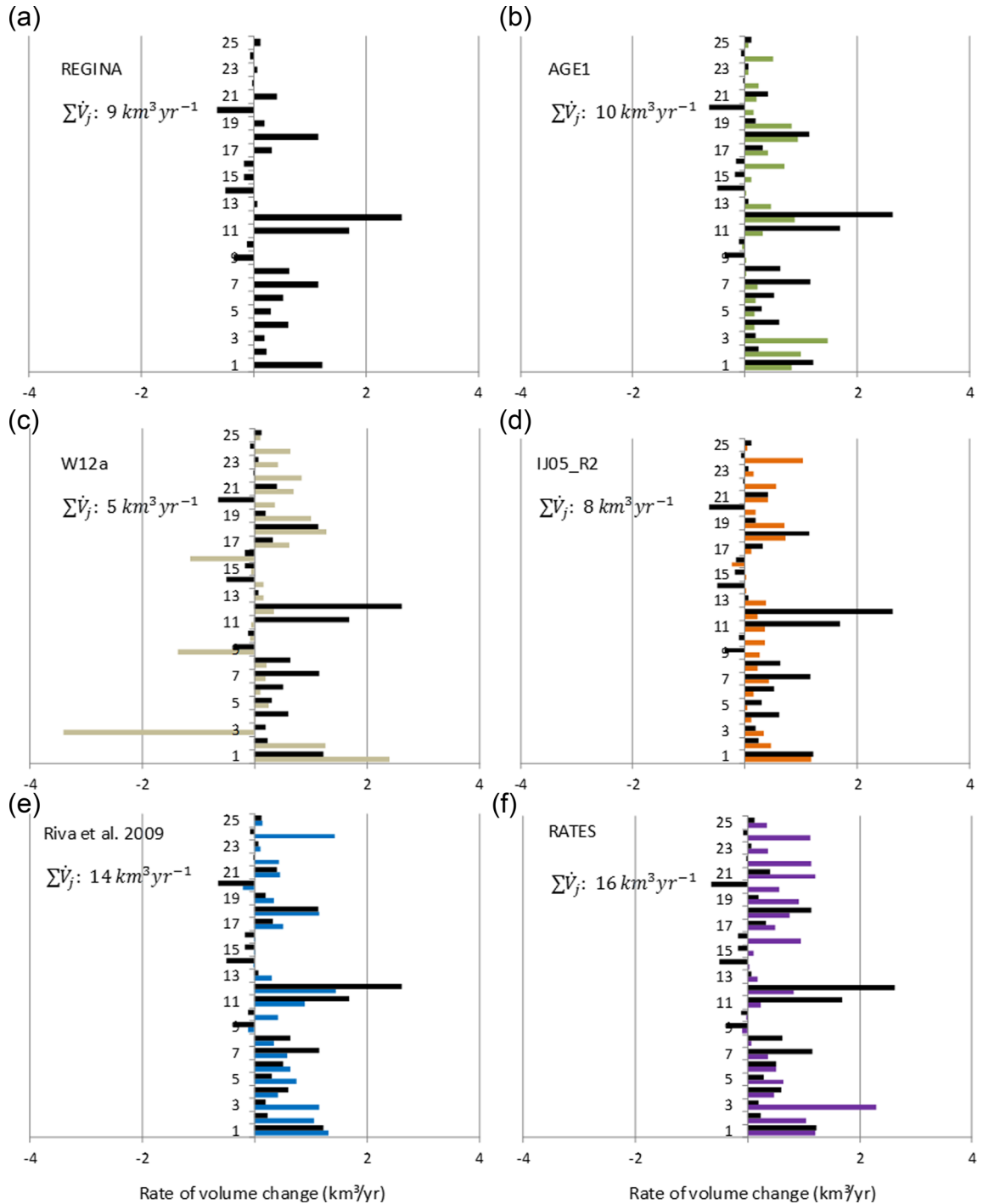
Figure 13. Rate of volume change (km³ yr⁻¹) for 25 Antarctic drainage sectors (Fig. 11), as obtained from (a) REGINA, (b) AGE1, (c) W12a, (d) IJ05_R2, (e) Riva *et al.* (2009) and (f) RATES. For comparison, the REGINA estimate is also indicated as black bars in (b)–(f).

reconcile GIA estimates and GIA forward models on a regional level.

5.3 Uncertainties and limitations of approach to estimate GIA

The combination approach involves three different types of space-geodetic data: elevation rates from altimetry, gravity-field rates from GRACE and uplift rates from GPS station records. Using a bootstrap approach with 1000 samples of the likelihood distribution (mean

and uncertainty) of the input data sets, we estimate the uncertainty of the GIA estimate (provided in Table 1), as well as the individual contributions shown Fig. 14. We perform the statistical sampling for individual data inputs, as well as for all inputs at the same time to account for possibly trade-off between errors from different sources.

Among these three data sets, elevation rates from altimetry clearly pose the largest contribution to the uncertainties of the inferred GIA estimate. One reason is the sampling problem, which was partially alleviated by combining ICESat (high accuracy in coastal regions) and Envisat (smaller bias in central Antarctica). Our results show
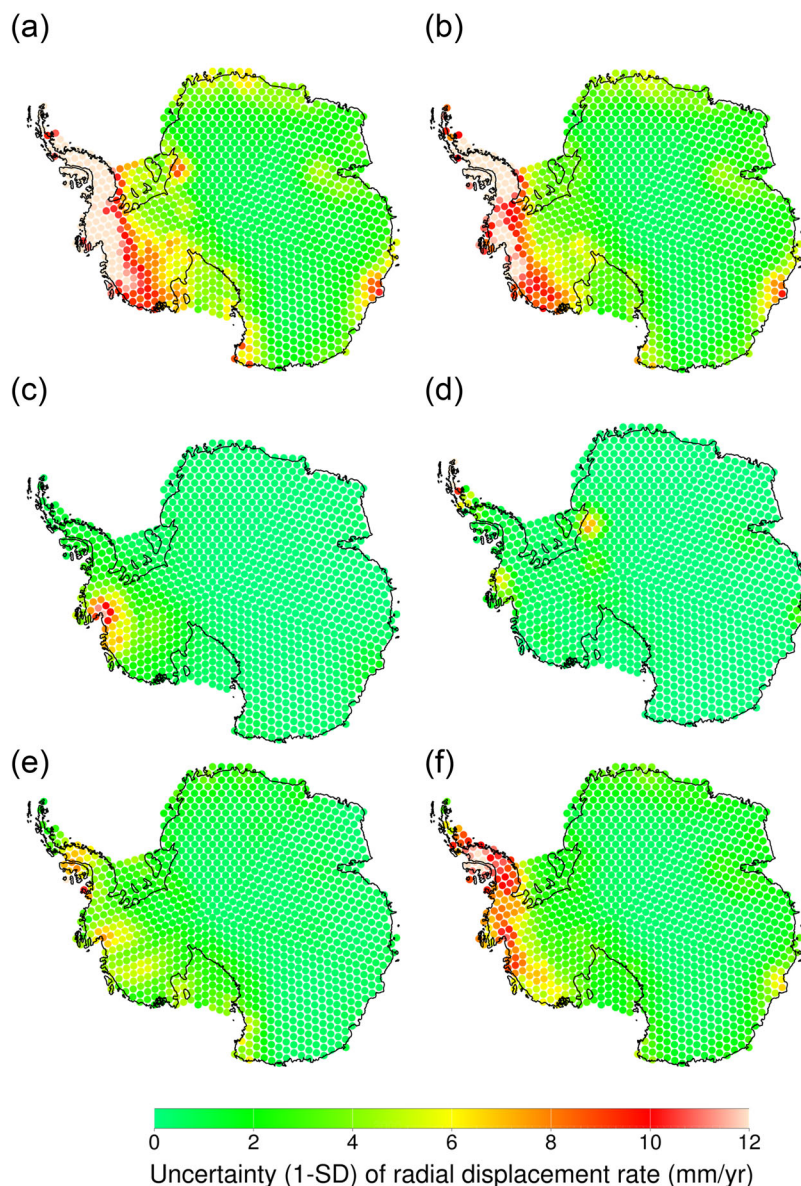
Figure 14. Uncertainty of the radial displacement of the GIA estimate and its individual contributions (mm yr^{-1}); (a) total uncertainty, and contribution from (b) altimetry (Envisat/ICESat; 2003–2009), (c) surface-density distribution, (d) GPS, (e) GRACE (magnitude of difference CSR RL05 and GFZ RL05) and (f) altimetry (Envisat/ICESat and CryoSat-2; 2003–2013; not used)

that further improvement is expected with CryoSat-2, particularly with its SARIn mode in coastal areas and possible swath processing, which provides denser elevation rate coverage around the ice margins where the largest rates are occurring (Gray *et al.* 2013). Here, however, we refrain from including the CryoSat-2 data in the inversion, because the time span of the data set was insufficient to retrieve annual rates of surface-elevation change comparable to the other data set. In future, however, an updated GIA estimate will likely be possible by appending the time spans of different altimetry measurements.

Another major source of uncertainty is the conversion of ice surface-elevation rates to mass rates (Fig. 14). In our approach, outlined in Section 2, elevation changes are first corrected for firn compaction and then attributed to changes in snow and ice based on a pre-defined mask; after that, remaining surface-mass signals are identified by the joint inversion of GRACE and GPS data, and

removed. However, this approach is limited by the spatial coverage of the GPS data.

Bedrock uplift rates derived from long-term and high-quality GPS records remain sparse in Antarctica (Fig. 4). Clearly, greater spatial coverage and longer time-series GPS data will improve the determination of GIA, as well as a better understanding of the spatial and temporal patterns of snow fall and ice-dynamic changes. Particularly, as many series of GPS sites provide only campaign measurements, further analysis is necessary of how interannual accumulation variations influence the derived rates and thus the GIA estimate. Nevertheless, Fig. 14 shows that except at a few sites, uplift rates from GPS are of sufficient accuracy to be valuable in a joint inversion GIA estimate, or for constraining GIA models.

The accuracy of the GRACE gravity fields is not a major limitation in the combination. In addition, it provides good spatial and temporal coverage. However, the coarse spatial resolution and

principal problem of leakage currently limits our ability to derive small-scale signatures of GIA (and ice-mass change) with confidence. Note that in the Antarctic Peninsula, where the GRACE resolution is well below the length scale of GIA (*ca.* 100 km, good GPS coverage is helping to constrain our GIA solution (Nield *et al.* 2012, 2014).

Finally, we have adopted viscoelastic response functions based on the equilibrium state for a constant unloading, removing all non-stationary characteristics of the temporal evolution. Even though the viscosity of the mantle underlying West Antarctica is probably low, this assumption may not be valid everywhere, which may lead to an overestimation of the recovered uplift rates. In addition, the Earth structure model adopted here (Priestley & McKenzie 2013) is subject to uncertainty. Nevertheless, we find that the choice of the Earth model parameters minimizes the misfit in both the GPS and gravity field rates and is therefore justified.

6 CONCLUSIONS

We have estimated GIA in Antarctica by the joint inversion of satellite altimetry, satellite gravimetry and GPS data. The inversion approach makes use of elastic and viscoelastic response functions to disc-load forcing, allowing us to partially account for lateral heterogeneous Earth structure in Antarctica and, in particular, a thin elastic lithosphere in West Antarctica. Including GPS uplift rates enables us to improve the separation of GIA and present-day ice-mass estimate, which initially rely on the surface-elevation rates from altimetry and an *a priori* snow/ice density distribution. Nevertheless, without further constraints on the spatial pattern of GIA, the uncertainty introduced by the altimetry data leads to a large uncertainty of the GIA estimate, also in West Antarctica (Fig. 14).

With the joint inversion, we successfully separate present-day ice-mass change and GIA, recovering a GIA estimate that is comparable in magnitude and spatial pattern to published GIA forward models, for example to IJ05 (Ivins *et al.* 2013) and W12a (Whitehouse *et al.* 2012) adopted in IMBIE (Shepherd *et al.* 2012). In total, the GIA-induced apparent mass change estimated is 55 ± 22 Gt yr^{-1}, which is identical to that obtained by an independent inversion approach using an entirely different methodology (RATES; Martín-Español *et al.* 2016a), and in support of IJ05 and W12a. However, regionally, and at the basin scale, large differences in rate and apparent mass change exist between the REGINA and other recent GIA corrections for Antarctica. This suggests that, although both GIA inversion estimates and forward models can provide consistent results at the continental scale, large discrepancies remain at the basin scale, and the attribution to East and West Antarctica.

Isolated large uplift rates measured by GPS in the Amundsen Sea Sector are reproduced by the joint inversion using viscoelastic response functions, which account for a weak Earth structure in West Antarctica. We estimate that about two-thirds of the measured uplift in the vicinity of the Thwaites and Smith/Pope/Kohler ice streams is caused by GIA. We suggest that this uplift is due to ice retreat within the past few centuries rather than unloading at the millennial timescale following the Last Glacial Maximum. Further GIA modeling studies are necessary to reconstruct the temporal evolution of the ice sheet leading to a viscoelastic response that satisfies our satellite-based GIA constraint for Antarctica.

Applying the REGINA GIA correction to trends from GRACE monthly solutions for 2003 January to 2016 March yields a ice-mass loss of the entire AIS of -141 ± 27 Gt yr^{-1}. The regional separation exhibits a slightly positive mass balance of 16 ± 17 Gt yr^{-1} for East Antarctica, a sustained negative balance of -30 ± 11 Gt yr^{-1} for the Antarctica Peninsula and increasingly negative mass balances currently at a rate of -127 ± 17 Gt yr^{-1} for West Antarctica.

REFERENCES

Abshire, J.B., Sun, X., Riris, H., Sirota, J.M., McGarry, J.F., Palm, S., Yi, D. & Liiva, P., 2005. Geoscience laser altimeter system (GLAS) on the ICESat Mission: on-orbit measurement performance, *Geophys. Res. Lett.,* **32**, L21S02, doi:10.1029/2005GL024028.

Altamimi, Z., Collilieux, X. & Métivier, L., 2011. ITRF2008: an improved solution of the international terrestrial reference frame, *J. Geod.,* **85**(8), 457–473.

An, M. *et al.*, 2015. S-velocity model and inferred Moho topography beneath the Antarctic Plate from Rayleigh waves, *J. geophys. Res.,* **120**(1), 359–383.

Bamber, J.L., Vaughan, D.G. & Joughin, I., 2000. Widespread complex flow in the interior of the Antarctic ice sheet, *Science,* **287**(5456), 1248–1250.

Bentley, M.J. *et al.*, 2014. A community-based geological reconstruction of Antarctic Ice Sheet deglaciation since the Last Glacial Maximum, *Quat. Sci. Rev.,* **100**, 1–9.

Bettadpur, S., 2012. Gravity Recovery and Climate Experiment UTCSR level-2 processing standards document, University of Texas at Austin, GRACE Doc, 327742, 16.

Bevis, M. *et al.*, 2009. Geodetic measurements of vertical crustal velocity in West Antarctica and the implications for ice mass balance, *Geochem. Geophys. Geosyst.,* **10**(10), doi:10.1029/2009GC002642.

Chambers, D.P. & Bonin, J.A., 2012. Evaluation of Release-05 GRACE time-variable gravity coefficients over the ocean, *Ocean Sci.,* **8**, 859–868.

Chen, J.L., Wilson, C.R. & Seo, K.W., 2009. S2 tide aliasing in GRACE time-variable gravity solutions, *J. Geod.,* **83**(7), 679–687.

DeMets, C., Calais, E. & Merkouriev, S., 2017. Reconciling geodetic and geological estimates of recent plate motion across the Southwest Indian Ridge, *Geophys. J. Int.,* **208**(1), 118–133.

Dziewonski, A.M. & Anderson, D.L., 1981. Preliminary reference Earth model, *Phys. Earth planet. Inter.,* **25**(4), 297–356.

Flament, T. & Rémy, F., 2012. Dynamic thinning of Antarctic glaciers from along-track repeat radar altimetry, *J. Glaciol.,* **58**(211), 830–840.

Frieler, K. *et al.*, 2015. Consistent evidence of increasing Antarctic accumulation with warming, *Nat. Clim. Change*, **5**(4), 348–352.

Gomez, N., Pollard, D. & Mitrovica, J.X., 2013. A 3-D coupled ice sheet–sea level model applied to Antarctica through the last 40 ky, *Earth planet. Sci. Lett.,* **384**, 88–99.

Gray, L., Burgess, D., Copland, L., Cullen, R., Galin, N., Hawley, R. & Helm, V., 2013. Interferometric swath processing of Cryosat data for glacial ice topography, *Cryosphere*, **7**(6), 1857–1867.

Groh, A., Ewert, H., Scheinert, M., Fritsche, M., Rülke, A., Richter, A. & Dietrich, R., 2012. An investigation of glacial isostatic adjustment over the Amundsen sea sector, West Antarctica, *Global Planet. Change*, **98–99**(0), 45–53.

Gunter, B.C., Didova, O., Riva, R.E.M., Ligtenberg, S.R.M., Lenaerts, J.T.M., King, M.A., van den Broeke, M. & Urban, T., 2014. Empirical estimation of present-day Antarctic glacial isostatic adjustment and ice mass change, *Cryosphere*, **8**(2), 743–760.

Hamed, K.H. & Rao, A.R., 1998. A modified Mann-Kendall trend test for autocorrelated data, *J. Hydrol.*, **204**(1–4), 182–196.

Hansen, S.E. *et al.*, 2014. Imaging the Antarctic mantle using adaptively parameterized P-wave tomography: evidence for heterogeneous structure beneath West Antarctica, *Earth planet. Sci. Lett.*, **408**, 66–78.

Heeszel, D.S. *et al.*, 2016. Upper mantle structure of central and West Antarctica from array analysis of Rayleigh wave phase velocities, *J. geophys. Res.*, **121**(3), 1758–1775.

Helm, V., Humbert, A. & Miller, H., 2014. Elevation and elevation change of Greenland and Antarctica derived from CryoSat-2, *Cryosphere*, **8**(4), 1539–1559.

Howat, I.M., Smith, B.E., Joughin, I. & Scambos, T.A., 2008. Rates of southeast Greenland ice volume loss from combined ICESat and ASTER observations, *Geophys. Res. Lett.*, **35**, L17505, doi:10.1029/2008GL034496.

Huybrechts, P., 2002. Sea-level changes at the LGM from ice-dynamic reconstructions of the Greenland and Antarctic ice sheets during the glacial cycles, *Quat. Sci. Rev.*, **21**(1), 203–231.

Ivins, E.R. & James, T.S., 2005. Antarctic glacial isostatic adjustment: a new assessment, *Antarct. Sci.*, **17**(04), 541–553.

Ivins, E.R., James, T.S., Wahr, J., Schrama, E.J.O., Landerer, F.W. & Simon, K.M., 2013. Antarctic contribution to sea level rise observed by GRACE with improved GIA correction, *J. geophys. Res.*, **118**, doi:10.1002/jgrb.50208.

King, M.A. & Santamaría-Gómez, A., 2016. Ongoing deformation of Antarctica following recent Great Earthquakes, *Geophys. Res. Lett.*, **43**, 1918–1927.

Kaufmann, G., 2002. Predictions of secular geoid changes from Late Pleistocene and Holocene Antarctic ice–ocean mass imbalance, *Geophys. J. Int.*, **148**, 340–347.

Konrad, H., Sasgen, I., Pollard, D. & Klemann, V., 2015. Potential of the Solid-Earth response for limiting long-term West Antarctic Ice Sheet retreat in a warming climate, *Earth planet. Sci. Lett.*, **432**, 254–264.

Lenaerts, J.T.M., van den Broeke, M.R., Berg, W.J., Meijgaard, E. & Kuipers Munneke, P., 2012. A new, high-resolution surface mass balance map of Antarctica (1979–2010) based on regional atmospheric climate modeling, *Geophys. Res. Lett.*, **39**, L04501, doi:10.1029/2011GL050713.

Ligtenberg, S.R.M., Helsen, M.M. & van den Broeke, M.R., 2011. An improved semi-empirical model for the densification of Antarctic firn, *Cryosphere*, **5**(4), 809–819.

Ligtenberg, S.R.M., Kuipers Munneke, P. & Van den Broeke, M.R., 2014. Present and future variations in Antarctic firn air content, *Cryosphere*, **8**(5), 1711–1723.

Mackintosh, A. *et al.*, 2011. Retreat of the East Antarctic ice sheet during the last glacial termination, *Nat. Geosci.*, **4**(3), 195–202.

Martín-Español, A. *et al.*, 2016a. Spatial and temporal Antarctic Ice Sheet mass trends, glacio-isostatic adjustment, and surface processes from a joint inversion of satellite altimeter, gravity, and GPS data, *J. geophys. Res.*, **121**, 182–200.

Martin-Español, A., King, M.A., Zammit-Mangion, A., Andrews, S.B., Moore, P. & Bamber, J.L., 2016b. An assessment of forward and inverse GIA solutions for Antarctica, *J. geophys. Res.*, **121**, 6947–6965.

Morelli, A. & Danesi, S., 2004. Seismological imaging of the Antarctic continental lithosphere: a review, *Glob. Planet. Change*, **42**(1), 155–165.

Nakada, M. & Lambeck, K., 1988. The melting history of the late Pleistocene Antarctic ice sheet, *Nature*, **333**, 36–40.

Nettles, M., Wallace, T.C. & Beck, S.L., 1999. The March 25, 1998 Antarctic plate Earthquake, *Geophys. Res. Lett.*, **26**(14), 2097–2100.

Nield, G.A. *et al.*, 2014. Rapid bedrock uplift in the Antarctic Peninsula explained by viscoelastic response to recent ice unloading, *Earth planet. Sci. Lett.*, **397**, 32–41.

Nield, G.A., Whitehouse, P.L., King, M.A., Clarke, P.J. & Bentley, M.J., 2012. Increased ice loading in the Antarctic Peninsula since the 1850s and its effect on glacial isostatic adjustment, *Geophys. Res. Lett.*, **39**, L17504, doi:10.1029/2012GL052559.

Peltier, W.R., 1994. Ice age paleotopography, *Science*, **265**, 195–201.

Peltier, W.R., 2004. Global glacial isostasy and the surface of the ice-age Earth: the ICE-5 G (VM2) model and GRACE, *Annu. Rev. Earth Planet. Sci.*, **32**, 111–149.

Priestley, K. & McKenzie, D., 2013. The relationship between shear wave velocity, temperature, attenuation and viscosity in the shallow part of the mantle, *Earth Planet. Sci. Lett.*, **381**, 78–91.

Rangelova, E. & Sideris, M.G., 2008. Contributions of terrestrial and GRACE data to the study of the secular geoid changes in North America, *J. Geodyn.*, **46**(3), 131–143.

Retzlaff, R. & Bentley, C., 1993. Timing of stagnation of Ice Stream C, West Antarctica, from short-pulse radar studies of buried surface crevasses, *J. Glaciol.*, **39**(133), 533–561.

Rignot, E., Bamber, J.L., Van Den Broeke, M.R., Davis, C., Li, Y., Van De Berg, W.J. & Van Meijgaard, E., 2008. Recent Antarctic ice mass loss from radar interferometry and regional climate modelling, *Nat. Geosci.*, **1**(2), 106–110.

Rignot, E., Mouginot, J. & Scheuchl, B., 2011a. Ice flow of the antarctic ice sheet, *Science*, **333**(6048), 1427–1430.

Rignot, E., Velicogna, I., Van den Broeke, M.R., Monaghan, A. & Lenaerts, J.T.M., 2011b. Acceleration of the contribution of the Greenland and Antarctic ice sheets to sea level rise, *Geophys. Res. Lett.*, **38**(5), doi:10.1029/2011GL046583.

Riva, R.E., *et al.*, 2009. Glacial isostatic adjustment over Antarctica from combined ICESat and GRACE satellite data, *Earth planet. Sci. Lett.*, **288**(3), 516–523.

Sasgen, I. *et al.*, 2017. Altimetry, gravimetry, GPS and viscoelastic modelling data for the joint inversion for glacial isostatic adjustment in Antarctica (ESA STSE Project REGINA), *Earth Syst. Sci. Data Discuss.*, submitted, doi:10.5194/essd-2017-46.

Sasgen, I., Martinec, Z. & Fleming, K., 2006. Wiener optimal filtering of GRACE data, *Stud. Geophys. Geod.*, **50**(4), 499–508.

Sasgen, I., Konrad, H., Ivins, E.R., Van den Broeke, M.R., Bamber, J.L., Martinec, Z. & Klemann, V., 2013. Antarctic ice-mass balance 2003 to 2012: regional reanalysis of GRACE satellite gravimetry measurements with improved estimate of glacial-isostatic adjustment based on GPS uplift rates, *Cryosphere*, **7**, 1499–1512.

Shepherd, A. *et al.*, 2012. A reconciled estimate of ice-sheet mass balance, *Science*, **338**(6111), 1183–1189.

Schroeder, D.M., Blankenship, D.D., Young, D.A. & Quartini, E., 2014. Evidence for elevated and spatially variable geothermal flux beneath the West Antarctic Ice Sheet, *Proc. Natl. Acad. Sci.*, **111**(25), 9070–9072.

Swenson, S. & Wahr, J., 2006. Post-processing removal of correlated errors in GRACE data, *Geophys. Res. Lett.*, **33**(8), L08402, doi:10.1029/2005GL025285.

Tarasov, L., Dyke, A.S., Neal, R.M. & Peltier, W.R., 2012. A data-calibrated distribution of deglacial chronologies for the North American ice complex from glaciological modeling, *Earth planet. Sci. Lett.*, **315**, 30–40.

Tikhonov, A.N. & Arsenin, V.Y., 1977. *Solution of Ill-posed Problems*. Winston & Sons.

Thomas, I.D. *et al.*, 2011. Widespread low rates of Antarctic glacial isostatic adjustment revealed by GPS observations, *Geophys. Res. Lett.*, **38**, L22302, doi:10.1029/2011GL049277.

Velicogna, I. & Wahr, J., 2002. A method for separating Antarctic postglacial rebound and ice mass balance using future ICESat Geoscience Laser Altimeter System, Gravity Recovery and Climate Experiment, and GPS satellite data, *J. geophys. Res.*, **107**(B10), 2263, doi:10.1029/2001JB000708.

Wahr, J., Wingham, D. & Bentley, C., 2000. A method of combining ICESat and GRACE satellite data to constrain Antarctic mass balance, *J. geophys. Res.*, **105**(7), 16 279–16 294.

Wan, H. *et al.*, 2013. The ICON-1.2 hydrostatic atmospheric dynamical core on triangular grids – Part 1: formulation and performance of the baseline version, *Geosci. Model Dev.,* **6,** 735–763.

Whitehouse, P.L., Bentley, M.J., Milne, G.A., King, M.A. & Thomas, I.D., 2012. A new glacial isostatic adjustment model for Antarctica: calibrated and tested using observations of relative sea-level change and present-day uplift rates, *Geophys. J. Int.,* **190,** 1464–1482.

Williams, S.D., Moore, P., King, M.A. & Whitehouse, P.L., 2014. Revisiting GRACE Antarctic ice mass trends and accelerations considering autocorrelation, *Earth planet. Sci. Lett.,* **385,** 12–21.

Wouters, B., Bonin, J.A., Chambers, D.P., Riva, R.E.M., Sasgen, I. & Wahr, J., 2014. GRACE, time-varying gravity, Earth system dynamics and climate change, *Rep. Prog. Phys.,* **77**(11), doi:10.1088/0034-4885/77/11/116801.

Wu, X. *et al.*, 2010. Simultaneous estimation of global present-day water transport and glacial isostatic adjustment, *Nat. Geosci.,* **3**(9), 642–646.

Wu, P. & Peltier, W.R., 1982. Viscous gravitational relaxation, *Geophys. J. R. astr. Soc.,* **70,** 435–485.

SUPPORTING INFORMATION

Supplementary data are available at *GJI* online.

Figure S1. Spatial distribution and histogram of disc radii for geodesic grid applied in this study.

Figure S2. Discs of geodesic grid attributed to continental ice (blue; 1022 discs) and ice-shelf areas (magenta; 153 discs) in Antarctica.

Figure S3. Effect of regularization parameter on smoothness of GIA estimate. Shown is the spatial rate of radial displacement (mm yr^{-1}) for the (a) regularization parameter $\lambda_N = 10^{1.5}$, optimal for CSR RL05, 2003–2009 (nominal solution shown in Fig. 8), (b) $\lambda_{N-} = \lambda_N \cdot 10^{-1.5}$ (less constrained; equivalent to *L*-curve optimal estimate), (c) $\lambda_{N+} = \lambda_N \cdot 10^{+3}$ (more constrained), as well as (d) the difference of (b) minus (a) and (e) the difference of (c) minus (a).

Figure S4. Effect of the thickness of the lithosphere on of GIA estimate. Shown is the spatial rate of radial displacement (mm yr^{-1})

for the threshold viscosity value of (a) $\eta_{LT} = 10^{22}$ Pa s (nominal solution shown in Fig. 8), (b) $\eta_{LT} = 10^{21}$ Pa s (*ca.* 10 km thinner lithosphere in West Antarctica), (c) $\eta_{LT} = 10^{23}$ Pa s (*ca.* 10 km thicker lithosphere in West Antarctica), as well as (d) the difference of (b) minus (a) and (e) the difference of (c) minus (a).

Figure S5. Predicted rate of geoid-height change and rate of radial displacement for the equilibrium state and different lithosphere thicknesses (30:30–90:90 km). The dashed lines represent the measurements from GRACE and GPS at BERP/TOMO, Amundsen Sea Embayment, West Antarctica. The adopted Earth structure at this location (according to Priestley & McKenzie 2013) is 80 km. The *a posteriori* validation of the lithosphere thickness purely from the data at this location is 80–90 km.

Figure S6. Rate of surface-ice elevation change from Envisat/ICESat (E/I; 2003–2009; same as Fig. 3), from CryoSat-2 (CS-2; 2010–2013), as well as the mean trend from both altimetry fields (E/I and CS-2; 2003–2013). Note that for grid nodes without CS-2 data, E/I for 2003–2009 are adopted.

Table S1. Misfit of the prediction and observation for difference processing centres, cut-off degrees and the time intervals 2003–2009 (short) and 2003–2013 (long). The estimates were derived based on the individually optimized regularization parameter.

Table S2. Total misfit of the prediction and observation for difference Earth structure parameters. Indicated is the threshold value applied to the 3-D viscosity profile of Priestley & McKenzie (2013) for the definition of the elastic lithosphere (higher threshold means thinner lithosphere thickness). The misfit for including a ductile layer in the crustal part of the lithosphere is also listed (not further used in this paper; see REGINA paper I, Sasgen *et al.* 2017). Results shown for GRACE solutions of CSR RL05, 2003–2009, cut-off degree 50.

Please note: Oxford University Press is not responsible for the content or functionality of any supporting materials supplied by the authors. Any queries (other than missing material) should be directed to the corresponding author for the paper.